Lawrence Berkeley National Laboratory
Recent Work

Title
A STUDY OF THE ii+ IN THE REACTION ii + p -> ii+ + ii- +n AT 365 AND 432 MeV

Permalink
https://escholarship.org/uc/item/19h0z2zb

Author
Solomon, Julius.

Publication Date
1963-01-17

eScholarship.org Powered by the California Digital Library
University of California

UCRL-10585

University of California

Ernest O. Lawrence Radiation Laboratory

TWO-WEEK LOAN COPY

This is a Library Circulating Copy which may be borrowed for two weeks. For a personal retention copy, call Tech. Info. Division, Ext. 5545

A STUDY OF THE π^+ IN THE REACTION $\pi^- + p \rightarrow \pi^+ + \pi^- + n$ AT 365 AND 432 MeV

Berkeley, California

DISCLAIMER

This document was prepared as an account of work sponsored by the United States Government. While this document is believed to contain correct information, neither the United States Government nor any agency thereof, nor the Regents of the University of California, nor any of their employees, makes any warranty, express or implied, or assumes any legal responsibility for the accuracy, completeness, or usefulness of any information, apparatus, product, or process disclosed, or represents that its use would not infringe privately owned rights. Reference herein to any specific commercial product, process, or service by its trade name, trademark, manufacturer, or otherwise, does not necessarily constitute or imply its endorsement, recommendation, or favoring by the United States Government or any agency thereof, or the Regents of the University of California. The views and opinions of authors expressed herein do not necessarily state or reflect those of the United States Government or any agency thereof or the Regents of the University of California.

Research and Development

UCRL-10585
UC-34 Physics
TID-4500 (19th Ed.)

UNIVERSITY OF CALIFORNIA
Lawrence Radiation Laboratory
Berkeley, California

Contract No. W-7405-eng-48

A STUDY OF THE π^+ IN THE REACTION $\pi^- + p \rightarrow \pi^+ + \pi^- + n$ AT 365 AND 432 MeV

Julius Solomon

(Ph. D. Thesis)

January 17, 1963

Printed in USA. Price $2.25. Available from the
Office of Technical Services
U. S. Department of Commerce
Washington 25, D.C.

A STUDY OF THE π^+ IN THE REACTION $\pi^- + p \rightarrow \pi^+ + \pi^- + n$ AT 365 AND 432 MeV

Contents

A STUDY OF THE π^+ IN THE REACTION $\pi^- + p \rightarrow \pi^+ + \pi^- + n$ AT 365 AND 432 MeV

Julius Solomon

Lawrence Radiation Laboratory
University of California
Berkeley, California

January 17, 1963

ABSTRACT

The differential distributions in energy and angle of the π^+ in the reaction $\pi^- + p \rightarrow \pi^+ + \pi^- + n$ have been measured with a scintillation counter telescope used for π^+ detection and a magnetic spectrometer for π^+ energy determination at π^- incident energies of 365 MeV and 432 MeV. At each of the laboratory-system angles 20, 50, 80, and 110 deg, π^+ were detected in scintillation counters placed after the spectrometer. This system covered a major portion of the kinematically allowed π^+ energy spectrum. The values of T and $\Delta T \Delta \Omega$ for each counter after the spectrometer were determined by suspended-wire measurements. Loss in π^+ detection efficiency due to the decay of the π was calculated. The e^+ contamination in the π^+ telescope was calculated and found to agree with a measurement made at 20 deg.

The total cross sections at 365 MeV, 2.39±0.20 mb, and at 432 MeV, 3.98±0.20 mb, are in agreement with other recent measurements. The angular distributions in the center-of-mass system (c. m.) are $d\sigma/d\Omega^*)_{365\ \mathrm{MeV}} = [(190\pm16) + (10\pm27)\cos\theta^*]\ \mu b/sr$ and $d\sigma/d\Omega^*)_{432\ \mathrm{MeV}} = [(317\pm16) + (35\pm26)\cos\theta^*]\ \mu b/sr$. At the higher energy the forward peaking of the π^+ is less pronounced than in a previous measurement of that characteristic. Both total cross section and angular distribution can be explained to present accuracy with two models: a $\pi\pi$ interaction model and an isobaric model. The π^+ c. m. energy distributions were observed to peak at lower energies than predicted by a phase-space distribution, thereby suggesting the presence of isobar formation in the final state. An attempt was made to fit the energy-spectrum data to an isobaric model using as many as three parameters. At 375 MeV moderately good fits are obtained, whereas at 432 MeV no reasonable fit to the measured energy spectrum could be found.

I. INTRODUCTION

The success of the Chew-Low static-model formalism[1] in explaining the so-called (3, 3) resonance (T = 3/2, J = 3/2) occurring at an energy $\omega_{\pi N}$ of about 1238 MeV in the π-nucleon system prompted several theoreticians[2] to extend that formalism to the process of single -π-meson production in πN collisions at low energies (up to 400 MeV incident pion kinetic energy). The reactions involved are

$$\pi^- + p \to \pi^+ + \pi^- + n, \quad (1)$$

$$\pi^- + p \to \pi^- + \pi^0 + p, \quad (2)$$

$$\pi^- + p \to \pi^0 + \pi^0 + n, \quad (3)$$

$$\pi^+ + p \to \pi^+ + \pi^+ + n, \quad (4)$$

and

$$\pi^+ + p \to \pi^+ + \pi^0 + p. \quad (5)$$

Experimental evidence not in agreement with theory first appeared in the study of Reaction (1) in 1958.[3] A second experiment, also Reaction (1), by Perkins et al.[4] in 1959 showed the following results:

(a) The measured total cross section was found to be higher by about a factor of 10 than that predicted by the static model.

(b) The total cross section was a sharply rising function of the incident pion energy.

(c) The angular distribution of the π^+ in the overall center-of-mass system was found to be forward peaked at 317 and 427 MeV, and was isotropic at 370 MeV.

Rodberg proposed that the size of the cross section might be due to an interaction of the incident π and a π in the nucleon cloud.[5] He considered only s- and p-wave $\pi\pi$ interactions. (For the incident energies 370 and 427 MeV the maximum values of $\omega_{\pi\pi}$, the energy in the $\pi\pi$ system, are respectively 416 and 460 MeV.) The sizable cross section at low energies suggested a large s-wave interaction, whereas the sharp rise as a function of energy required a p wave. He performed the calculation in the zero-range approximation, assuming that only the one-meson-exchange term contributed. He considered the possibility that one of the final pions rescattered off the nucleon in the (3, 3) state, and concluded that the effect was small because the value of

$\omega_{\pi N}$ averages 100 MeV below the resonance value at these incident energies. $\omega_{\pi N\ \max}$ at 370 MeV is about 1220 MeV and at 427 about 1255 MeV.

For a given partial wave in the $\pi\pi$ system the model predicted a pion angular distribution in the over-all center of mass frame favoring forward angles, and an energy distribution "tending toward slightly higher energies than predicted by phase space." The isotropy of the angular distribution at 370 MeV (at which energy the p wave may become important) could be due to an interference of the s- and p-wave interactions. Some expectations for Rodberg's model at higher energies (about 400 MeV), where the p wave should be most important, were that

(a) a forward-backward asymmetry should appear in the $\pi\pi$ c.m. system,

(b) higher $\pi\pi$ energies should be favored,

(c) the ratio of the cross section for Reaction (1) to that for Reaction (2) should approach 2.

The results found by Perkins et al., and Rodberg's proposal, were sufficiently interesting that in 1960 our group at the Lawrence Radiation Laboratory decided to concentrate on the measurement of πp inelastic reactions at low energies. The study of $\pi^- + p \rightarrow \pi^+ + \pi^- + n$ (Reaction 1) reported in this thesis was undertaken to verify Perkins's results, to improve the statistics of the measurement, and in particular to study the π^+ energy distributions, because the last are sensitive to any $\pi^- n$ final-state interactions. Subsequently Reactions (2) and (3) were also measured. They are discussed in Sec. VII. A.

Perkins et al. had used the $\pi^+ \rightarrow \mu^+ + \overline{\nu}$ decay scheme to verify the presence of the π^+, and a range scheme to measure its energy. The efficiency of their π^+ telescope averaged about 25%. In our measurement a magnetic spectrometer and a scintillation counter telescope having an efficiency of about 90% were used to identify positively charged particles and to measure their momentum. Protons were excluded from the π^+ telescope by range requirements.

A second conjecture regarding Perkins's data was advanced in 1961 by V. V. Anisovich.[6] He could fit all of Perkins's data by using a model that did not include a $\pi\pi$ interaction, but required only the previously mentioned basic (3, 3) resonance. The final-state interaction was sufficiently strong to explain the sharp rise in the cross section as a function of energy. At 432 MeV, our highest incident π^- energy, the maximum $\omega_{\pi N}$ attainable was 1240 MeV, so that the greater part of the data lies below the peak of the resonance. Because $\pi^- n$ is a pure $T = 3/2$ state whereas $\pi^+ n$ is both $T = 3/2$ and $T = 1/2$, there is a greater probability for the isobar to be formed between the π^- and the neutron than between the π^+ and the neutron. At 365 MeV π^- incident energy the total center-of-mass energy, E^*, is 1359 MeV and at 432 MeV incident energy $E^* = 1405$ MeV. After the formation of a 1238±50-MeV isobar very little energy is left over for the recoil π^+.

The main difference, therefore, between the $\pi\pi$ model and the isobar model that could be determined from this experiment would be in the π^+ energy spectra. The isobar model would favor low c. m. energies for the π^+, while the $\pi\pi$ model would favor higher c. m. energies. The angular distributions cannot be simply inferred, and are discussed in Sec. VII.

II. PION BEAM

A. Design

This experiment was performed during July and August 1960 in the meson cave of the 184-inch synchrocyclotron at the Lawrence Radiation Laboratory.

A π^- was produced in the reaction $p + n \rightarrow p + p + \pi^-$ when the internal 732-MeV proton beam struck a beryllium target. The π^- "spray" was then bent out of the vacuum tank by the magnetic field of the cyclotron, and a chosen momentum interval was collected by a quadrupole doublet Q1 (see Figs. 1 and 2) and rendered parallel through the meson wheel. The meson wheel is an 8-ft-diameter iron cylinder, 1 ft high. The wheel contains a slot 12 in. wide, 8 in. high, and 8 ft long through which the emerging pion beam is passed. Since the center about which the wheel rotates is fixed, the slot must be aligned at the angle that is optimum for the pion energy desired. The wheel's angle is defined as the angle the slot makes with the normal to the cyclotron tank wall (Fig. 1). The particles emerging from the cyclotron were momentum-analyzed by the bending magnet (also in Fig. 1). The beam was then focused onto a liquid hydrogen target by a second doublet quadrupole Q2. Two collimators were used to further define the beam spot and keep spray off the aluminum flanges of the hydrogen target.

A number of considerations were important in the design of the beam:

(a) Placement of the Be target and the wheel angle setting were necessarily different for different momentum beams because of the effect of the cyclotron magnetic field on the emerging negative pion beams.

(b) Assuming a phase-space distribution for the π^--production process, we expected the greatest flux of π^- for 0° production, and for the target at cyclotron radius = 82 in., the radius at which the internal proton beam achieves maximum energy.

(c) The π^+-detection system required a circular area 10 ft in diameter. Such an area was available only in the northwest corner of the meson cave. Therefore, the approximate location of the hydrogen target was predetermined.

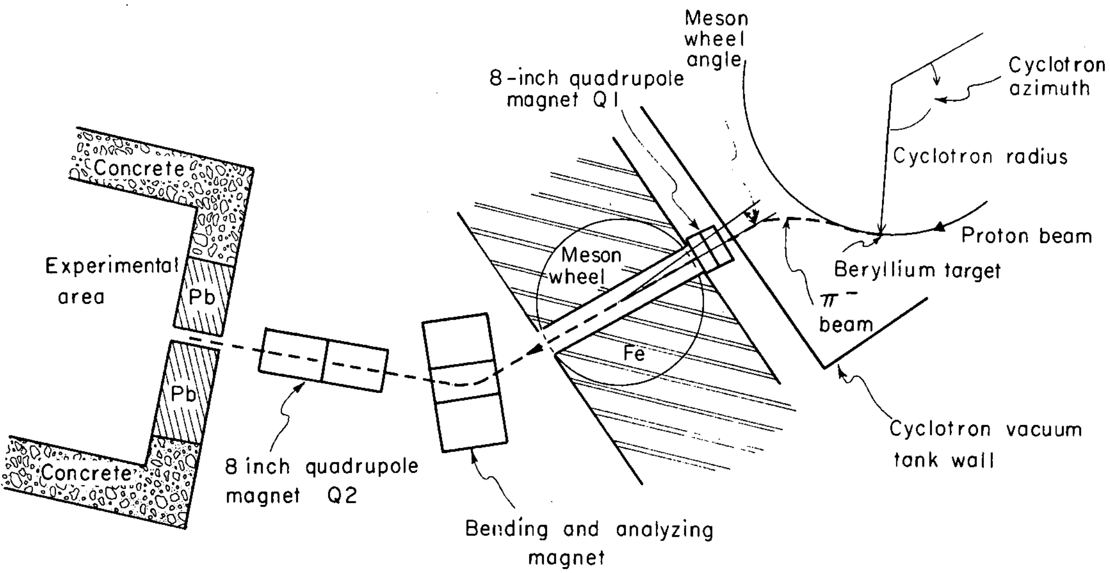

Fig. 1. Diagram of meson cave beam setup.
Detail of experimental area is given in Fig. 5.

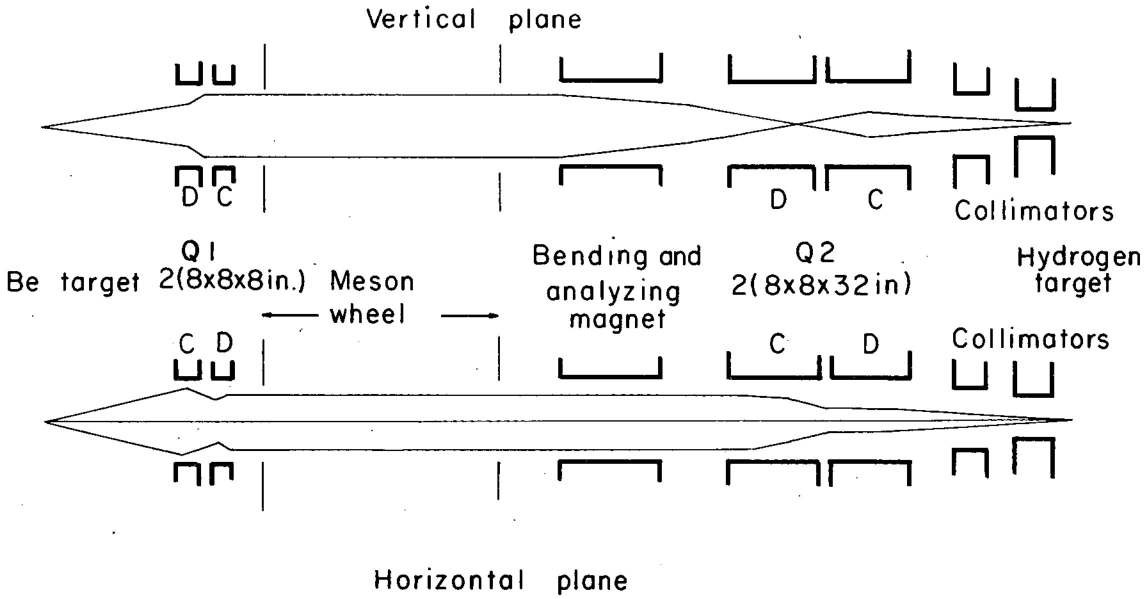

MU-29640

Fig. 2. Diagram of beam optics.
Q = quadrupole magnet
C = quadrupole element converging the beam.
D = quadrupole element diverging the beam.

(d) It was undesirable to alter the experimental setup, mainly the LH_2 target position, when changing π^- incident energies from 365 to 432 MeV.

By tracing pion orbits through the known cyclotron magnetic field we determined the best setting of the wheel angle for the Be target at cyclotron radius = 82 in. and for 0° production of the π^- off the target. Since the center of the meson wheel is fixed, the target position had to be adjusted in azimuth. (Fig. 1) Further orbit analysis yielded the effective object distance of the target from quadrupole Q1, which was used to calculate the Q1 currents and polarities required to render the beam parallel inside the meson wheel. The decision to render the beam parallel in the wheel was made because Q1 was not strong enough to bring pion beams of the desired energy to a focus.

The angle of bend for each pion energy was then completely determined by the calculated wheel setting and the desired location for the liquid hydrogen target. To change over from one energy to the other necessitated small movements of Q1 and of the bending magnet and a relocation of the Be target.

Bending-magnet currents giving the desired bend for the selected pion momenta were experimentally determined before the actual run by suspended-wire measurement.[7] Quadrupole currents were experimentally optimized to give the best beam spot and maximum pion flux at the hydrogen target. A sample beam profile taken at the target position (432 MeV π^- energy) is shown in Fig. 3.

B. Beam Energy Determination

Integral range curves of π^- in copper absorber were obtained for both π^- incident energies. Figure 4 shows the range curve for 365 MeV. Straight lines AB and BC were drawn under the assumption of a rectangular energy distribution for both the π^- and μ^-. The straight line segment left of A is an approximation of a small part of the exponential π-absorption curve. Point A is the break between the curve for π^- nuclear interaction loss and the actual stopping of pions

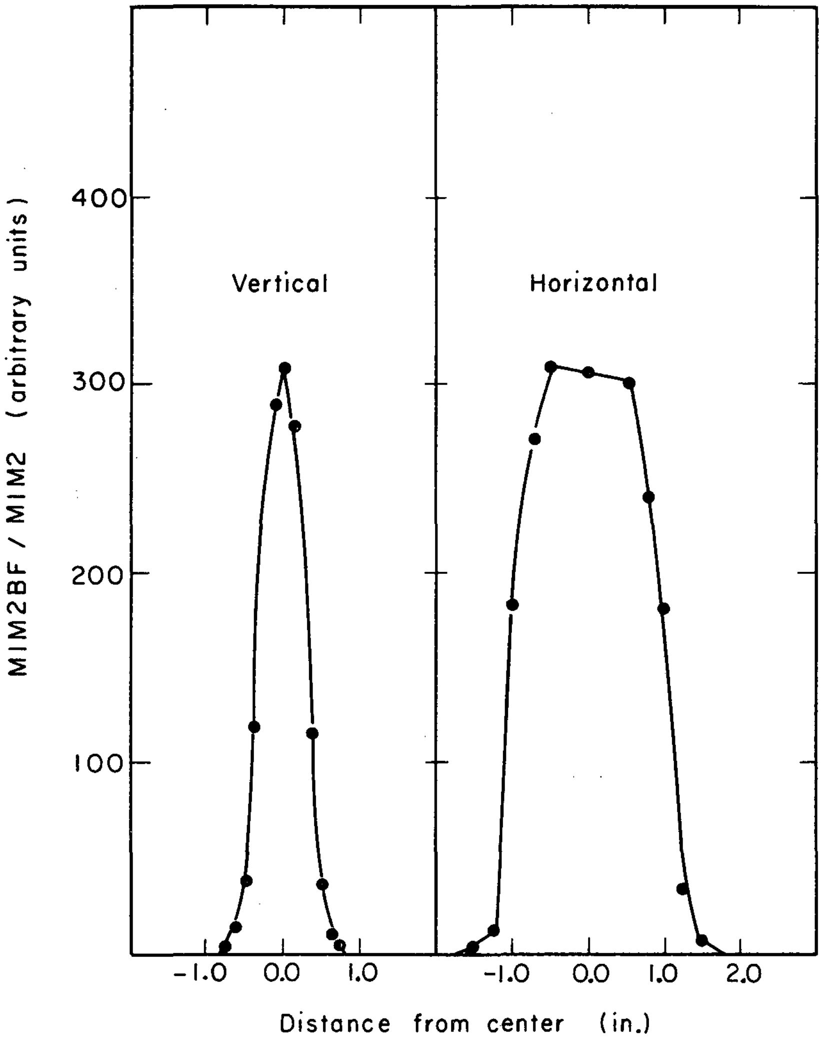

MU-29641

Fig. 3. Beam profiles at the hydrogen target position for 432 MeV incident energy.

M1M2BF = number of coincidences of monitor and beam finder counters.

M1M2 = number of monitor counts.

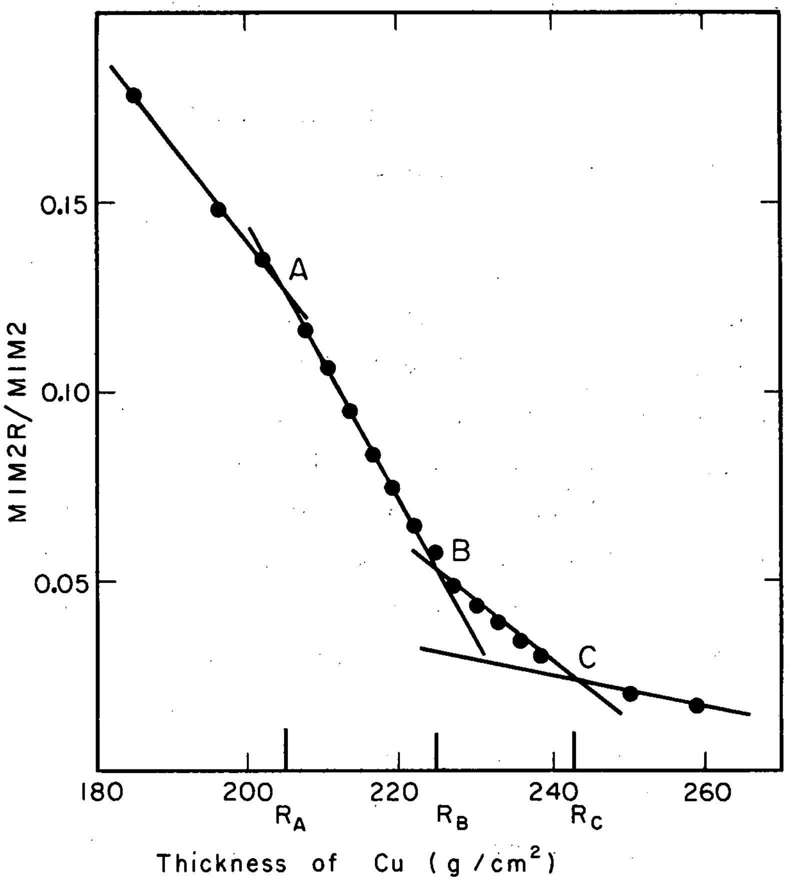

MU-29642

Fig. 4. Integral range curve for 365-MeV π^- beam.
M1M2R = number of coincidences of monitor and range counter.
M1M2 = number of monitor counts.

due to range. B is the break between the π-stopping curve and the μ-stopping curve. The energy limits of the π^- were determined from range-energy tables using points R_A and R_B.[8] The central energy was taken halfway between the two limiting energies. The energy spread given by the range-curve determination agrees with the spread expected from consideration of the magnet's properties and the geometry (± 3%).

C. Beam Contamination

The beam contaminations consisted of μ^- and e^-. To the right of point R_B in Fig. 4 only particles of range greater than 380 MeV remain (μ's and e's). Point R_C marks the limit of μ^- range. To the right of R_C positrons and electrons remain. However, these are not a measure of the actual e^- contamination. They are mainly due to charge exchange in the copper absorber which eventually results in pairs that produce showers in the copper. (For the reactions involved see Sec. V. B.) An order-of-magnitude estimate of the contribution to the total number of electrons and positrons at point R_C of the range curve (Fig. 4) due to the charge-exchange-caused showers gave for the ordinate at R_C a calculated value of 0.016, whereas 0.023 was the measured value. The e^- contamination was not measured during the run, but was measured for a similar type of beam with a gas Cerenkov counter and determined to be 0.3%.[9]

The muon contamination due to muons of range greater than 225 g/cm^2 was obtained by subtracting the electron background at point B' from the muons plus electrons at point B in the range curve.

Muons arising from π^- decays before the bending magnet were momentum-analyzed and those within the defined momentum interval were included in the above measurement. Muons arising from the decay of π^- after the bending magnet have a spectrum of energies. Only the fraction of these whose range was greater than the π range were included in the measurement. The μ contamination after the magnet was calculated and combined with results of range-curve measurement to give a total muon contamination.

The properties of the beam are listed in Table I.

Table I. Beam properties.

	Energy (MeV)	
	365 ± 15	432 ± 15
μ^- Contamination (%)	4.1±0.41	3.8±0.38
e^- Contamination (%)	0.3±0.3	0.3±0.3
Flux (π/minute)	3×10^6	1×10^6

III. EXPERIMENTAL APPARATUS

A. Hydrogen Target

The liquid hydrogen target used in this experiment was of the type described by Newhart et al.[10] The liquid hydrogen was stored in a reservoir surrounded by a vacuum, an aluminum heat shield, and a liquid nitrogen reservoir in order to minimize the boiling of the hydrogen.

The flask was a 2-in.-diameter cylinder extending 4 in. along its central axis, which was parallel to the beam (Fig. 5). The walls of the flask were 6-mil Mylar. The flask was suspended in a chamber having an "aluminized" Mylar window 4 in. high and subtending a circular arc of 240 deg. The flask walls and window were made thin so as to reduce the ratio of background to the hydrogen-derived particles.

B. Beam Monitor

The π^- beam at the cyclotron was produced at the rate of 64 cycles per second. Within each cycle the beam was spread over a period of about 400 microseconds. The beam "spill" had a fine structure about 13 nsec wide every 54 nsec within the 400 μsec. Our beam design gave us an increase by a factor of three to five over intensities previously achieved in the meson cave. This increase in intensity also gave us the problem of monitoring the beam accurately. It put us in the region where the probability of getting two π^- in one 13-nsec fine-structure pulse was about 10%. This probability will be referred to as "beam bunching" or just "bunching."

Two scintillation counters, called the "beam monitor" counters, detected the incident π^- beam before it entered the hydrogen target (see Fig. 5). Since a pulse from each of the counters was required to turn on the electronics of the π^+ telescope, the counters defined the beam size at the target. At high beam levels--approx 3×10^6/min--the beam monitor counters would count low by as much as 10% owing to bunching. Therefore we also set up a two-counter telescope designated "Scattering Monitor," which monitored the particles scattered off our ion chamber. This telescope did not have the bunching problem because

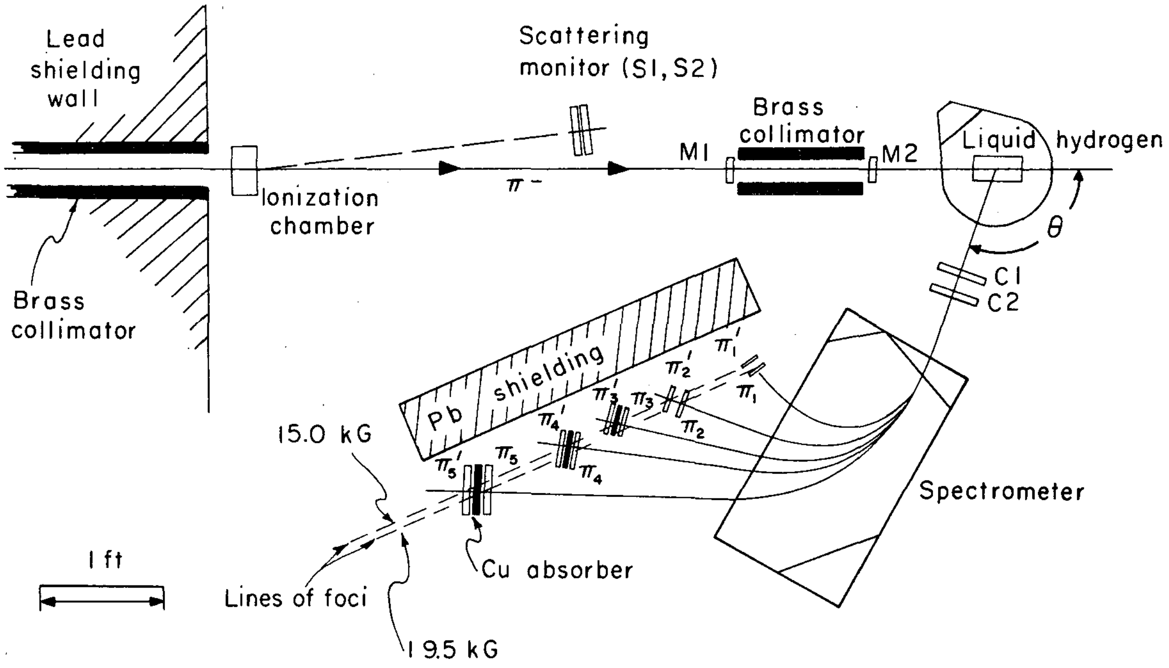

MU-29643

Fig. 5. Diagram of experimental area.

its rate was approximately 1/20 that of the beam monitor. The response of our ion chamber (Fig. 5) was found to drift, with a rate that was easily measurable but that varied with time. Since it was impractical to make drift measurements every few hours, the ion chamber was not used as a monitor but was used to check the linear response of the other two monitors as a function of beam level. Figure 6 shows that the response of the scattering monitor was nearly linear as a function of beam level whereas that of the monitor counters was not. With the aid of the scattering monitor a bunching correction was made to the beam monitor, giving the true number of π^- passing through the beam monitor counters.

Table II summarizes the three pieces of beam-monitoring equipment.

Table II. Beam-monitor equipment.

Monitor	Dimensions (in.)			Description
Ion chamber	4 (diameter)			Lucite frame; three 2-mil Al plates, two 5-mil Al walls. Pressure: 2 lb; mixture 96% A, 4% CO_2.
	Height	Width	Thickness	
Beam Monitor				
M1	1	2	1/8	Plastic scintillator
M2	3/4	1-3/4	1/8	Plastic scintillator
Scattering monitor				
S1	5	5	1/2	Plastic scintillator
S2	5	5	1/2	Plastic scintillator

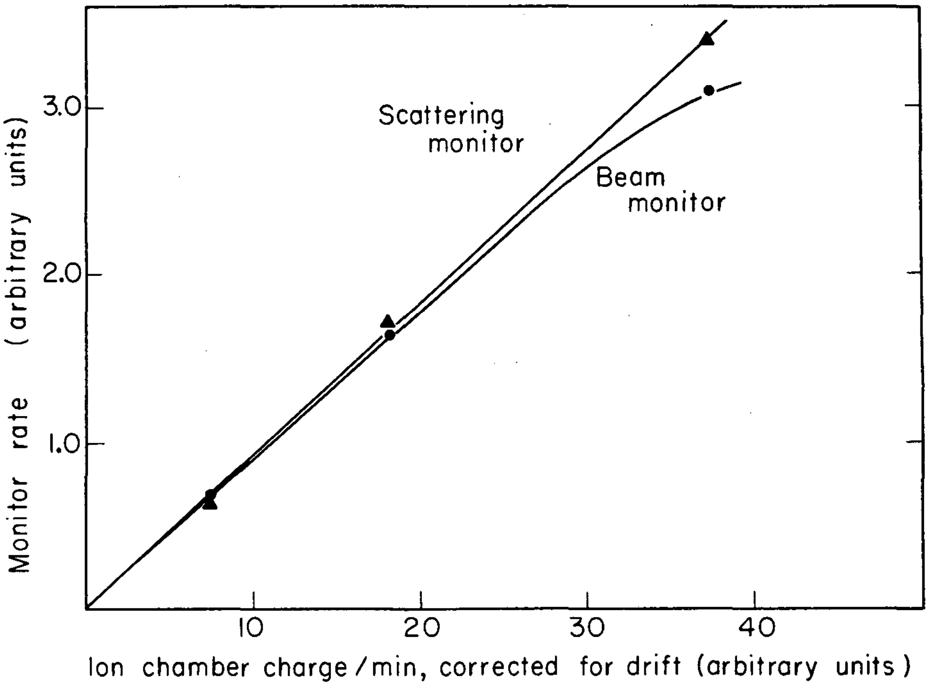

MU-29644

Fig. 6. Linearity test of beam monitor and scattering monitor as a function of beam level.

C. π^+ Telescope and Spectrometer

One aim of this experiment was to detect the π^+ with a much greater efficiency than in the measurement of this reaction by Perkins et al.[4] They detected the π^+ by its decay, and determined its energy from its range in copper. Their efficiency averaged 25%. Our π^+ telescope used a magnetic spectrometer both for momentum analysis and for identification of the charge of the particle. The losses in efficiency were due to (a) absorption and multiple scattering of the π^+ in parts of the telescope (see Fig. 5), and (b) decay of the π^+ to $\mu^+ + \bar{\nu}$.

The telescope consisted of two scintillation counters, C1 and C2, before the spectrometer magnet, and five sets of two scintillators, π and π', after the magnet. Protons were not counted in the final $\pi\pi'$ counters because copper sheets sufficiently thick to stop them were placed between the latter counters. The extra absorber lowered our efficiency by only 2%. This is because a pion and a proton of the same momentum in our momentum region have ranges in the ratio of approximately 100:1.[8]

What the π^+ telescope did not do was to separate the π^+ from the μ^+ or e^+. The μ^+ that came about from the decay of the π^+ could not experimentally be eliminated, and therefore a correction described in Sec. V. C. 1 and Appendix A was applied to the data.

The e^+ contamination came from the conversion of γ rays arising from the decay of the π^0. The reactions involved in e^+ production are

$$\left.\begin{array}{l}\pi^- + p \rightarrow \pi^0 + n \\ \pi^- + p \rightarrow \pi^0 + \pi^0 + n \\ \pi^- + p \rightarrow \pi^- + \pi^0 + p\end{array}\right\} \quad \left.\begin{array}{l}\pi^0 \rightarrow \gamma + \gamma \\ \quad\;\; \rightarrow \gamma + e^+ + e^-\end{array}\right\} \quad \gamma \rightarrow e^+ + e^- . \tag{6}$$

An attempt was made to experimentally eliminate the e^+ by use of a 1-cm-thick glycerol Cerenkov counter. It was inserted between counters C1 and C2 with the intention of detecting positrons but not the π^+. However, this counter failed because of poor light collection. Some of our early data were taken with the Cerenkov counter in place.

These were compared with data taken later without the Cerenkov counter, and they agree within the statistics of either measurement. The e^+ contamination correction is described in Sec. V. B.

The physical characteristics of the π counter telescope are given in Table III. All scintillators used in this experiment were a mixture of terphenyl and polystyrene. The light pipes were lucite. The scintillators were viewed by RCA 6810A phototubes.

Table III. π^+ telescope scintillation counters.

Counter	Height (in.)	Width (in.)	Thickness (in).
C1, C2	1.0	4.0	1/8
$\pi\pi'$	12.0	2.0	1/4
	12.0	2.5	1/4
	12.0	3.0	1/4
	12.0	3.5	1/4
	12.0	4.0	1/4

The π^+ spectrometer was a 13X24-in. C magnet with pole pieces shaped to give vertical focusing action at the entrance edge (see Fig. 5). At the exit edge there was either vertical focusing or defocusing depending upon the π^+ exit angle. The gap width was 4 in. Data were taken at two magnet-current settings in order to accommodate the range in the momenta of the π^+, which varied as a function of laboratory-system angle. (See Table IV.)

Table IV. Spectrometer properties.

Angle (lab) (deg)	Magnet current (A)	Magnetic field (gauss)	T_π (MeV)
20, 50	998.24	19,500	40 to 180
80, 110	561.3	15,000	15 to 110

The magnet, along with the π counter telescope, was mounted on a steel frame fastened to a 4-ft -diameter gun mount in order to facilitate change of the angle of observation of the π^+. The hydrogen target was suspended from above over the center of rotation of the gun mount.

Suspended-wire measurements were made prior to the run to determine where the $\pi\pi'$ counters should be placed with respect to the magnet. In an analogous case in optics, if a light source of variable frequency emits light that passes through a prism a separate image is produced for each frequency of light emitted. If the frequency range is continuous the locus of the image of the source's center is a smooth curve. In our case we determined by suspended-wire measurements a curve of momentum foci, assuming a point target source located at the position of the center of the hydrogen target. During the run the $\pi\pi'$ counters were positioned along this line perpendicular to the ray of the desired momentum that had passed through the center of counter C2. Figure 5 shows where the measured line of foci lay with respect to the magnet for both magnetic field values.

The sizes of the $\pi\pi'$ counters tangent to the line of foci were varied so that the $\pi\pi'$ counter momentum acceptances were about ±10% at all π^+ energies. The height of the $\pi\pi'$ counters was chosen to be 12 in. so that any possible vertical defocusing action at the exit edge would not cause the π^+ to miss the rear counters.

The suspended-wire method was also used to determine that the correct maximum vertical size of counters C1 and C2 was 1 in. The requirement was that no π^+ produced by an incident π^- passing through M2 (3/4-in. vertical size) should pass through C2 and be able to hit the magnet pole pieces. The limiting aperture of the telescope in the vertical direction, was therefore, counter C2.

D. Electronics

The block diagram of the electronics used is found in Fig. 7. A beam-monitor count was given by a coincidence M1M2 in coincidence circuit W1. The sum of accidentals and of the bunching correction for W1 was monitored simultaneously in W2 where M1 was delayed 54 nsec (1 fine-structure pulse) with respect to M2. The accidentals (about 5% of W2) were calculated from the measured singles rates and the resolving time of the circuit (4 nsec) and subtracted from the total to give the bunching correction. Since accidentals were small, W2 essentially measured the probability of two pions' being in adjacent fine-structure pulses, which is the same as the probability of two pions' being in the same fine-structure pulse.

A "common" pulse occurred if there was a coincidence M1M2C1C2 in W3. This coincidence circuit registered all the particles passing through C1 and C2 produced in the target by the incident π^- beam. The common pulse was then placed in coincidence with all the separate $\pi\pi'$ combinations in circuits E1 through E5, verifying that a positively charged particle had passed through the spectrometer. "Accidental" circuits E1A to E5A required the same coincidences except that the "common" pulse was delayed 108 nsec, or 2 fine-structure widths. This delay was taken as 108 nsec rather than 54 nsec because the time acceptance of the E circuits was about 50 nsec.

The π accidental rate averaged 4% of the real rate ("reals") at 20 deg, where the number of common pulses was greatest owing to the forward peaking of the elastic scattering. At 110 deg the accidentals were highest, averaging 6% of the reals, because at this angle the $\pi\pi'$ counters were closest to the actual beam line. At the intermediate angles the accidentals averaged 1% of the reals. The lead shielding wall next to the $\pi\pi'$ counters (Fig. 5) was essential in keeping the accidentals low. Bunching in the π^+ telescope was negligible, since the probability of detecting one π^+ was very small.

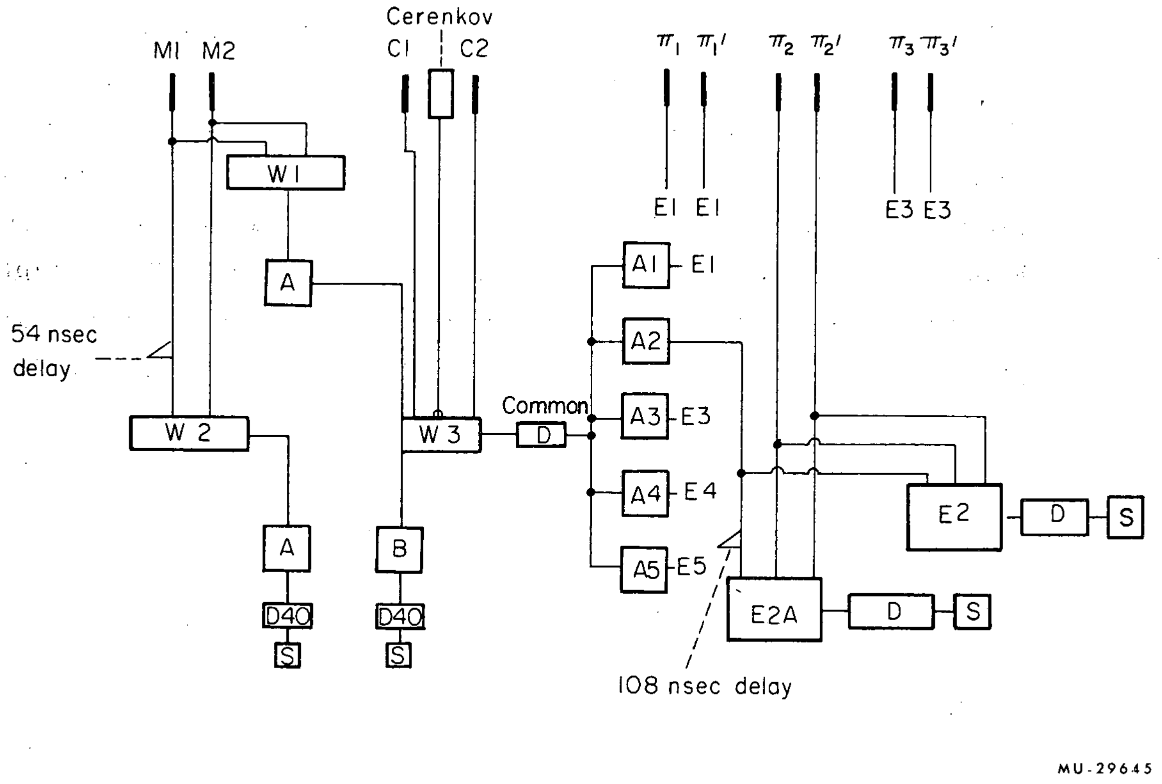

Fig. 7. Electronics block diagram. Descriptions of circuits may be found in the Radiation Laboratory Counting Handbook, UCRL-3307 (Rev.).
W - three-channel fast coincidence circuit (Wenzel)
E - three-channel coincidence and anticoincidence unit (Evans)
D - three-channel amplitude discriminator (Perez-Mendez)
D40 - special 40-Mc discriminator--scale-of-8 prescaler (Jackson)
S - scalers
A - Hewlett-Packard A distributed amplifier
B - Hewlett-Packard B distributed amplifier
⊿ - added cable delay

IV. EXPERIMENTAL PROCEDURE

A. π^+ Measurement

It was necessary to experimentally set the location of the internal Be target before each day's running, owing to the inability of the cyclotron crew to exactly reproduce the target setting. The target position was determined by maximizing the beam monitor rate in counters M1 and M2.

The π data were taken with the hydrogen target flask both full and empty. The "flask-empty" counts were due to reactions in the material surrounding the target, and the "full" counts were due to reactions from both the hydrogen and the surrounding material. The "in-out ratio," or the ratio of the π counts with the hydrogen target full to π counts with the flask empty, averaged 2:1 at backward angles and 3:1 at forward angles. The ratio of target-full to target-empty running time was taken as the square root of the "in-out" ratio in order to optimize the counting statistics at each point. The target was filled or emptied every two hours to assure as much as possible that any change in running conditions be present in both target-full and target-empty data. To minimize the rejection of runs due to electronic equipment failure the data were recorded every hour or so. All the runs were checked for consistency and the runs having obvious mistakes were rejected. Less than 1% of all runs were rejected in this way. For each π counter at each lab angle all the separate runs were added together and the net yield per unit monitor, Y, along with its statistical uncertainty, ΔY, were calculated by

$$Y = \frac{F - A_f}{M_f} - \frac{E - A_e}{M_e} \quad , \qquad (7)$$

$$\Delta Y = \left[\frac{F + A_f}{M_f{}^2} + \frac{E + A_e}{M_e{}^2} \right]^{1/2} \quad , \qquad (8)$$

where

F = number of π counts recorded with the hydrogen target full,

E = number of π counts recorded with the hydrogen target empty,

A_f = number of π accidental counts recorded with the hydrogen target full,

A_e = number of π accidental counts recorded with the hydrogen target empty,

M_f = number of M1M2 counts recorded with the hydrogen target full,

M_e = number of M1M2 counts recorded with the hydrogen target empty.

B. $\Delta T \Delta \Omega$ Measurement

The solid angle and energy acceptance for each $\pi\pi'$ counter at each lab angle were measured by the suspended-wire method. Figure 8 shows the experimental setup and gives the coordinate system used. Our method determined the acceptance, i. e. the product $\Delta T \Delta \Omega$ of the $\pi\pi'$ counters for several points of origin in the target. The acceptance was then averaged over the target to give $\Delta T \Delta \Omega$ of each counter for the whole target.

The method used was based on the fact that the limiting vertical aperture of the telescope and spectrometer system was counter C2 (see Sec. III. C) and on the assumption that any difference between the energy acceptance of a $\pi\pi'$ counter for rays out of the median plane of the spectrometer and that for rays in the median plane could be neglected, since the maximum deviation out of the plane was ±6 degrees. Under these conditions the acceptance of $\pi\pi'$ was determined in terms of a coordinate system x' with respect to counter C2. It was advantageous to do it in this way rather than by projecting C2 back on the $\pi\pi'$ counter because the useful area of C2 directly determines the solid angle subtended by $\pi\pi'$. The method also had the advantage that it was simple to determine the desired product $\Delta T \Delta \Omega$ by tracing out the limits of the acceptance in the T-x' coordinate system and transforming to a T-Ω coordinate system.

The first step was to measure for a single point of origin in the target, as a function of x' (in cm), the position in counter C2 (Fig. 8), the energy spread $\Delta T(x')$ of π's passing through x' accepted by the $\pi\pi'$

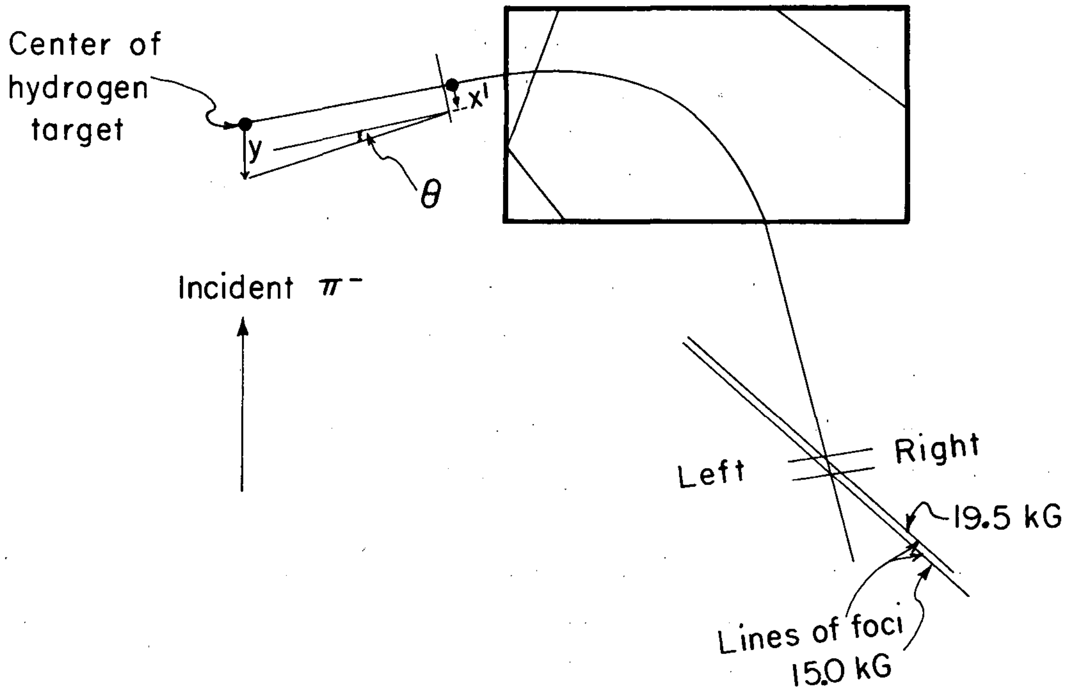

MU-29646

Fig. 8. Diagram of suspended-wire setup for $\Delta T \Delta \Omega$ determination.

counters. The limiting energies were determined by two suspended wires originating at the target point and passing over x'. One of these (the lower energy) was terminated at the left side of the counter and the other (higher energy) at the right side of $\pi\pi'$.

Figure 9 gives the results of typical suspended-wire measurements made with the wire origin at the position of the center of the hydrogen target. In Fig. 9 the abscissa is the initial π kinetic energy and the ordinate x' (in cm) is the position at which the wire passed over C2 when at equilibrium. C2's center is at $x' = 0.0$. Curves A and B are the extremities of C2. The curves labeled T_{left} and T_{right} refer to the maximum and minimum energies mentioned.

The region enclosed by the four curves A, B, T_{left}, and T_{right} is the acceptance of the $\pi\pi'$ counter in the T-x' coordinate system. Lines of constant x' included in that region give the aforementioned quantity $\Delta T(x')$, while lines of constant T in that region give the part of C2 in the horizontal plane that is imaged at the back counter for that value of the pion energy. Since the limiting vertical aperture of the system is counter C2, its vertical image must necessarily fall inside the $\pi\pi'$ counter. The area of C2 that determines the useful solid angle for that $\pi\pi'$ counter is then the product of the height of counter C2 and the length of x' that falls inside the above region. For example, in Fig. 9 at $x' = 2.0$ we have $\Delta T(x') = (79.4 - 63.6)$ MeV, and at $T = 68$ MeV the portion of C2 that contributes to the solid angle extends from $x' = -2.25$ to $x' = 5.08$.

In order to transform the acceptance of the counter from a T-x' coordinate system to a T-Ω coordinate system and determine the desired $\Delta T \Delta\Omega$, each value of $\Delta T(x')$ was weighted with a factor $h dx' \cos\theta(x', y)/r^2(x', y)$, and an integration was performed over x', where

h = height of counter C2 = 1.0 in.,

$\overline{r}$ = vector from target point y to counter point x', and

θ = angle between the normal to area hdx' and the vector r.

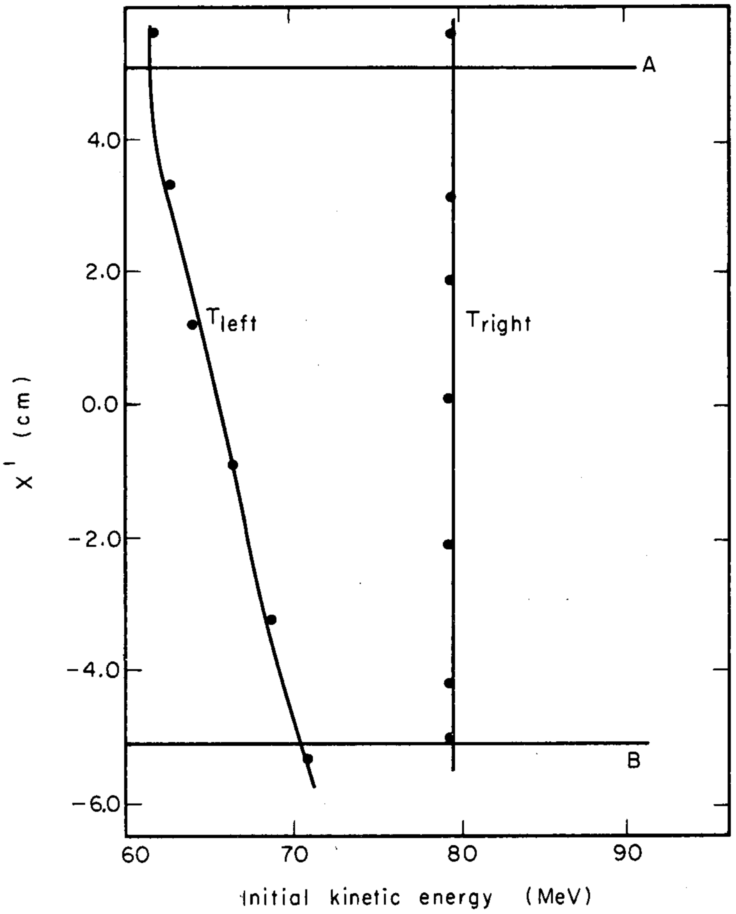

MU-29647

Fig. 9. Initial π^+ kinetic energy vs equilibrium position at counter C2 for counter $\pi\pi'_2$ at 50°, 365 MeV incident energy, originating at target center y = 0. A, B, are the extremities of counter C2. Left, Right refer to the edges of $\pi\pi'_2$.

In this step we have used the assumption that $\Delta T(x')$ was the same for rays both in and out of the median plane. The expression for $\Delta T \Delta \Omega$ of the $\pi\pi'$ counter for a target point y was

$$\Delta T \Delta \Omega(y) = \int_{\text{Counter C2}} dx' \, h \, \frac{\cos\theta\,(x', y)}{r^2(x', y)} \left[T_{\text{right}}\,(x', y) - T_{\text{left}}\,(x', y) \right] \quad (9)$$

Equation (9) was integrated numerically on the IBM 7090 computer.

The third step was to determine $\Delta T \Delta \Omega$ for the whole target by averaging the measured $\Delta T \Delta \Omega(y)$ over the target. The averaging was performed by integrating that function over y and dividing by the target length. The integration over the target length was performed on the basis of three values at $y = 0$, $+2$, and -2, the center and ends of the target. The uncertainty in the determination of the value of Eq. (9) was then mainly due to the y integration. Two methods were considered which usually gave the same answer to within 2%. Method 1 was to draw two trapezoids by connecting the three points with straight lines. Method 2 was to draw a smooth curve between the three points and to integrate by hand. The values of $\Delta T \Delta \Omega(y)$, the result of the x' integration, as a function of y fcr $\pi\pi'_2$ at 50 deg, 365 MeV is shown in Fig. 10 along with the curves for the two methods described.

The previous treatment had assumed that a line target was a good representation of the actual cylindrical target. This was a fair approximation because 75% of the beam was contained within a circle of radius 0.6 in. about the central axis of the cylinder. This distance is small compared with the distance to counter C2, so that the average value of $1/r^2$ was approximately equal to $1/r^2_{\text{av}}$.

The uncertainty assigned to the $\Delta T \Delta \Omega$ in most cases was taken as twice the difference between the values of Methods 1 and 2 described above. This uncertainty averaged 4%. However, some of the measurements when plotted for consistency showed a definite systematic error. The uncertainties assigned to these points were as high as 10%.

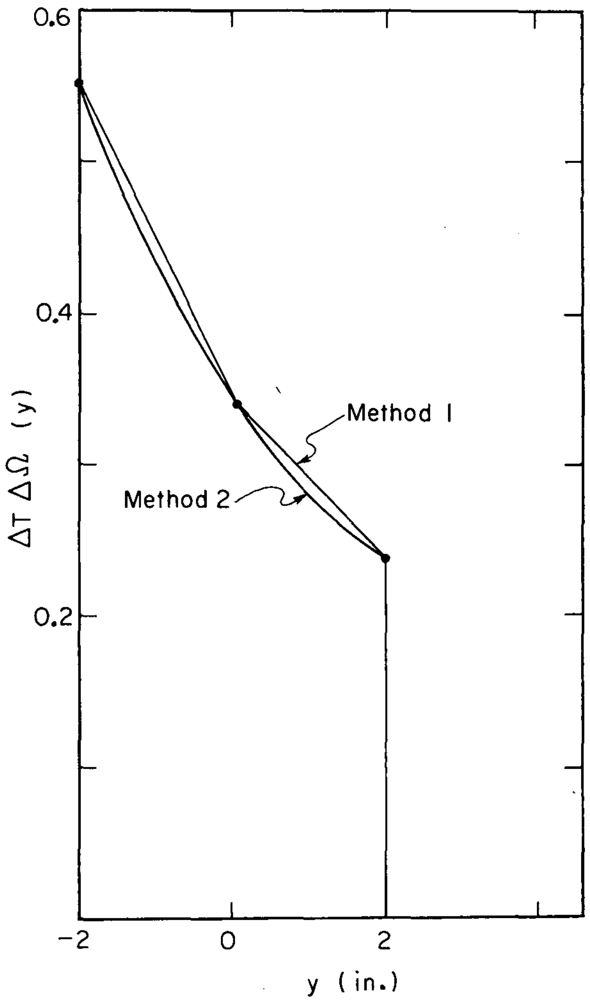

MU-29648

Fig. 10. Plot of $\Delta T \Delta \Omega(y)$ vs y for counter $\pi\pi'_2$ at 50°, 365 MeV incident energy.
Integration Method 1 gave $\Delta T \Delta \Omega = 0.370$ MeV-sr and Integration Method 2 gave $\Delta T \Delta \Omega = 0.366$ MeV-sr. (See text for description of methods.)

V. CORRECTIONS

A. Beam Monitor Correction

Three steps were required to determine the actual number of π^- striking the liquid hydrogen target.

(a) The total number of all beam particles passing through M1, M2, and the target was determined by correcting the number of monitor counts as given by the M1M2 coincidence circuit for bunching, i.e., the number of times that two or more particles occurred in one fine-structure pulse. Bunching was measured by delaying M2 by one fine-structure pulse with respect to M1 as described in Section III. D.

(b) The corrected number of monitor counts was adjusted to take into consideration the μ and electron contaminations (see Table I in Sec. II).

(c) The measured beam profiles in Fig. 2 were used to determine that 8±1% of the counted beam completely missed the hydrogen flask.

At 432 MeV the bunching, the coincidence between M1 and M2 delayed 54 nsec, was measured for each run. The bunching correction at this energy averaged 2.5±0.5% of the measured M1M2. The 365-MeV data, however, did not have the bunching measured for each run, but series of runs at several beam levels were made periodically wherein the bunching, the number of monitor counts, and the scattering monitor were recorded. Each series was considered a calibration run. By use of the best available measurements of the bunching at 365 MeV, the bunching correction was made and a value for the corrected monitor, $(M1M2)_{corr}$, determined. Next the fractional deviation

$$\left| \frac{\Delta(M1M2_{corr}/S1S2)}{(M1M2_{corr}/S1S2)} \right|$$

was evaluated for each calibration run. A weighted average of the fractional deviations gave an average deviation of 2%. The bunching-correction uncertainty was taken to be 2%. The average bunching correction at 365 MeV was 10%.

B. Positron Contamination

Since the charge-exchange cross section in the 350- to 450-MeV energy region is about ten times the total inelastic cross section for π^0 production, the contaminating positrons arose mainly from the decay of the charge-exchange π^0. The reactions involved are

$$\pi^- + p \rightarrow \pi^0 + n, \qquad (10)$$

$$\pi^0 \rightarrow \gamma + \gamma, \qquad (11)$$

or

$$\pi^0 \rightarrow \gamma + e^+ + e^-, \qquad (12)$$

and

$$\gamma \rightarrow e^+ + e^-. \qquad (13)$$

The decay of the π^0, Reactions (11) and (12), occurs through Reaction (11) about 99% of the time and through Reaction (12) about 1% of the time. The pair produced in Reaction (12) is called the "Dalitz" pair.[11] The pair produced in Reaction (13) comes from the conversion of a γ ray in the target or some of its surrounding material. Thus it was called the "conversion" pair.

1. Calculation of Positron Contamination

The differential distribution of γ's arising from the charge-exchange π^0 decay, $d^2\sigma/dkd\Omega$, is given by Squire[12] in terms of the expansion of the π^0 c.m. cross section, $d\sigma/d\Omega^*)_{\pi^0} = \sum a_n P_n(\alpha)$, (14)

where α = cosine of π_0 c.m. angle,

P_n = the nth-order Legendre polynomial,

a_n = coefficient of nth term,

k = γ momentum,

and Ω = unit of solid angle (lab).

The a's were taken from the data of Caris.[13] The values of the a's at 432 MeV were extrapolated from his data at lower energies; the values used at 365 MeV were interpolated from his data.

The probability of converting a γ of momentum k is given by the pair-production attenuation coefficient of the materials as a function of k.[14, 15]

The distribution of e^+ momenta, p_{e^+}, arising from the conversion of a γ ray of momentum k was taken to be isotropic from $p_{e^+} = 0.0$ to $p_{e^+} = k$. The actual distribution bulges slightly at the high and low ends,[15] but this was neglected in order to simplify the calculation.

The distribution of $d^2\sigma/dp_{e^+}d\Omega$ due to γ conversion was then

$$\frac{d^2\sigma^c}{dp_{e^+}d\Omega} = \int_{p_{e^+}}^{k_{max}} \frac{d^2\sigma}{dk'd\Omega}\ \frac{\alpha t(k')}{k'}\ dk' \ , \tag{15}$$

where $\alpha t(k')$ = pair-production attenuation coefficient multiplied by the thickness of absorber averaged over all the different materials as a function of γ momentum k';

$\frac{d^2\sigma^c}{dT_\pi d\Omega} = \frac{E_\pi}{P_\pi}\ \frac{d^2\sigma^c}{dp_{e^+}d\Omega}$ = probability per unit pion energy per steradian of producing by γ conversion and e^+ having momentum and direction the same as those of the π^+,

E_π = pion energy, and

P_π = pion momentum.

A similar calculation was performed to determine $\frac{d^2\sigma^d}{dT_\pi d\Omega}$ under the simplifying assumption of zero mass for the e^+. In the energy region dealt with (60 to 300 MeV) this was not a bad assumption. Starting from known angular and energy distribution of the Dalitz e^+ in the π^0 rest frame,[10] we transformed to the center-of-mass frame. This distribution was weighted by $d\sigma/d\Omega^*)_{\pi^0}$ of Caris and transformed to the laboratory system to yield $d^2\sigma^d/dE_{e^+}d\Omega$, and again transformed to $\frac{d^2\sigma^d}{dT_\pi d\Omega}$.

The results of both these calculations at 365 MeV are shown in Figs. 11 and 12.

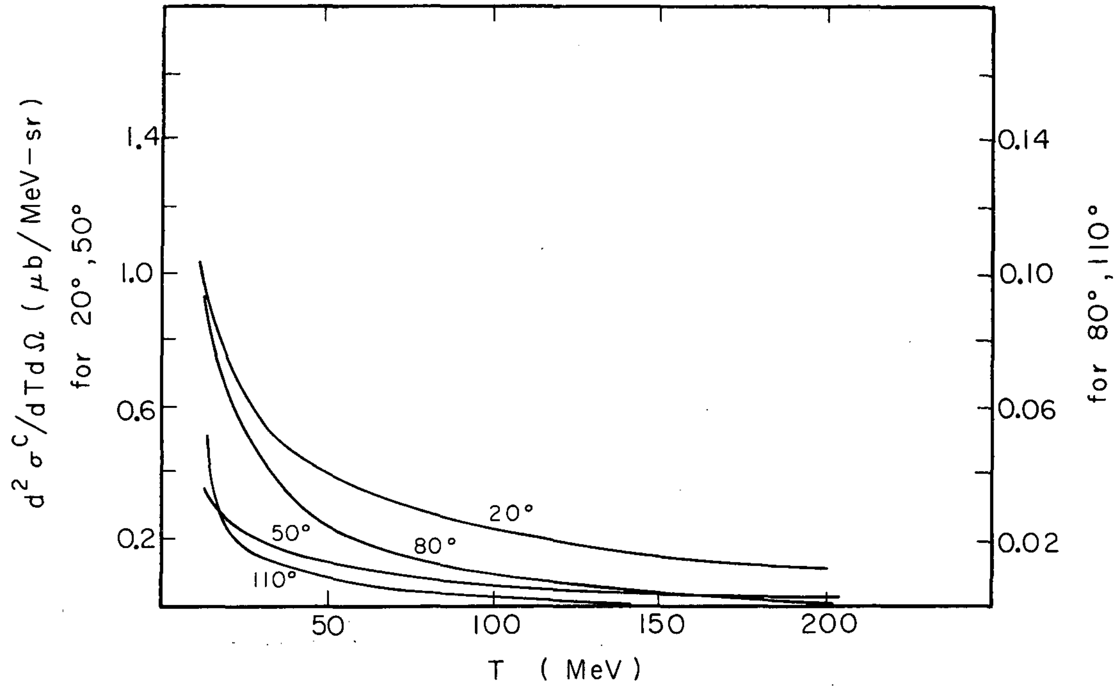

MU-29665

Fig. 11. Plot of $d^2\sigma^c/dTd\Omega$ vs T_π for 365 MeV incident energy.

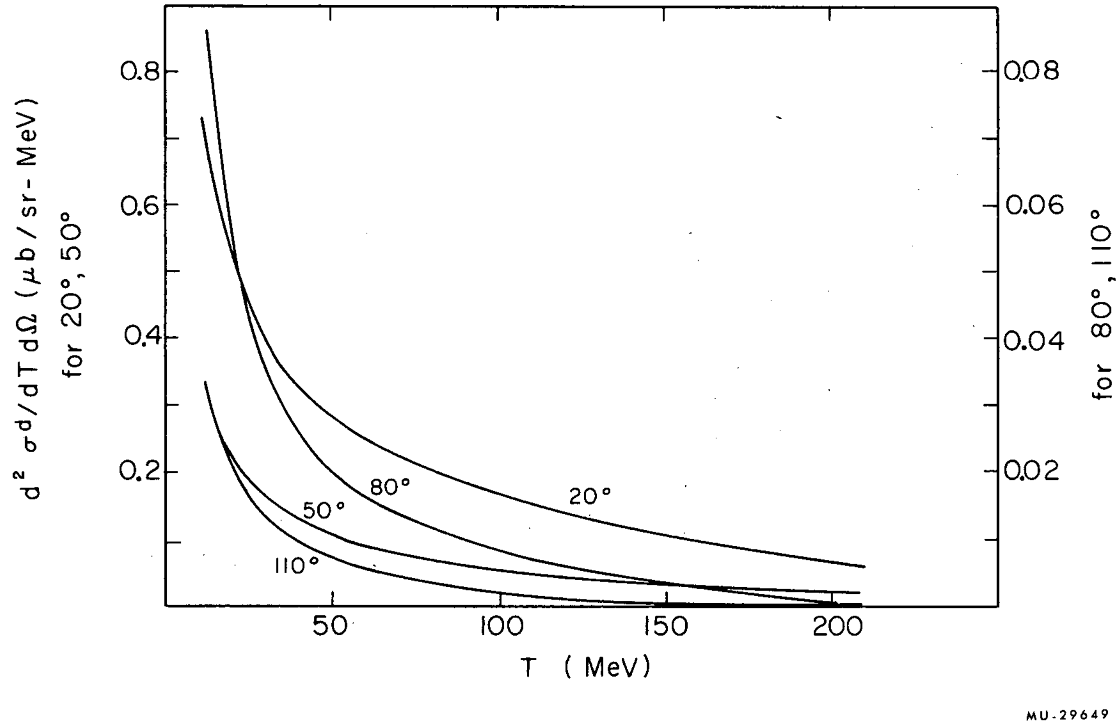

Fig. 12. Plot of $d^2\sigma^d/dTd\Omega$ vs T_π for 365 MeV incident energy.

2. Measurement of e^+ Contamination Due to γ Conversion

Table V gives as a function of lab angle the values of

$$\frac{d\sigma}{d\Omega} = \int_{k_{min}}^{k_{max}} \frac{d^2\sigma}{dk d\Omega} dk, \tag{17}$$

where

$\frac{d^2\sigma}{d\Omega dk}$ is the probability of producing a γ momentum k per solid angle $d\Omega$ per MeV/c, and $d\sigma/d\Omega$ is that probability integrated over all allowable γ energies.[12]

Table V. Cross sections for production of γ by charge exchange.

Angle (lab) (deg)	k_{max} (MeV/c)	k_{min} (MeV/c)	$d\sigma/d\Omega$ (mb/sr)
20	494.0	17.7	10.18
50	429.2	15.4	3.87
80	355.7	12.8	0.982
110	299.3	10.7	0.452

Table V shows that our positron contamination was probably greatest at 20 deg. An experimental determination of the positron contamination was made at that angle for both incident π^- energies. The π data were recorded while either 24 mils or 48 mils of Cu was pasted on the front of counter C1. The copper added more material in which the γ could convert and had less than 1% effect upon the overall π efficiency. By fitting with a straight line the π counting rate at the three points (0, 0.024, and 0.048 in. Cu expressed in terms of equivalent target thickness), we were able to determine from the slope of the line the positron contamination due to conversion in the target. With the π^+ telescope at 20 deg, and with 365 MeV incident energy, the measurements and best fit for $\pi\pi'_2$ are shown in Fig. 13. The error flags represent the statistical uncertainty of the measurements.

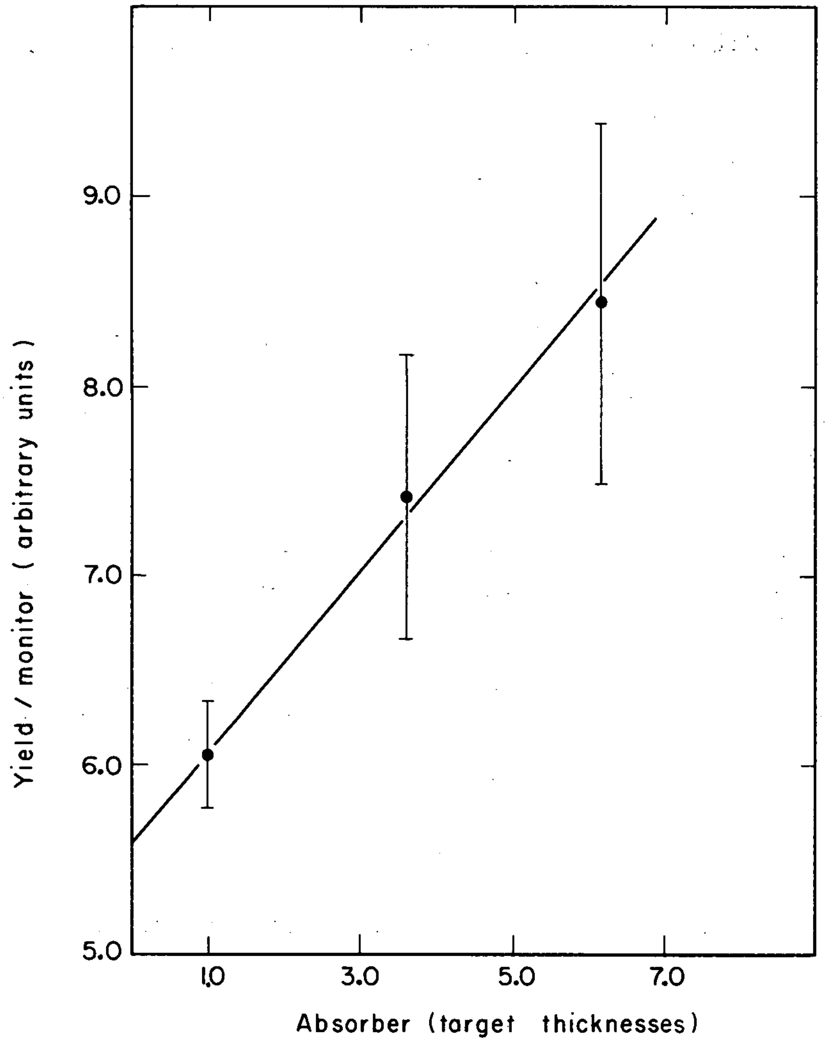

Fig. 13. Measurement of e^+ contamination due to γ conversion for $\pi\pi'_2$ at 20° for 365 MeV incident energy.

3. e^+-Contamination Correction

Figure 14 is a comparison between the measured and calculated contaminations due to conversion at 20 deg (lab) angle for 365 MeV. The uncertainty assigned to the calculation was given by the uncertainty in the a's of the charge-exchange cross-section measurements used for the calculation. The uncertainty assigned to the measured contamination was given by the error matrix of the straight-line fit to the measurements. Since measured and calculated contaminations for conversion agreed reasonably well at 20 deg, the correction for positron contamination at all angles was made by using the calculated values. The above agreement was about the same for 432 MeV, 20 deg.

The calculated total contaminations were 16% at 20 deg for 365 MeV, at 9% at 20 deg for 432 MeV. The contamination dropped off rapidly with increasing angle.

C. π^+ Telescope Efficiency

1. Efficiency Loss Due to the Decay $\pi^+ \rightarrow \mu^+ + \overline{\nu}$

The π^+ decays to a $\mu^+ + \overline{\nu}$ with a measured mean life equal to $2.55 \pm 0.03 \times 10^{-8}$ sec.[16] The path traveled by the π^+ in the spectrometer was long enough so that 12 to 18% of the π^+ (depending upon its energy) decayed in flight.

The fraction of pions headed for a particular counter but lost due to decay in flight was calculated on the IBM 7090 computer. The losses depended upon the total path traveled in the spectrometer, hence upon the point of origin, the direction, and the energy of the π^+ leaving the target. The average loss in a π counter was calculated in the following way:

(a) For each pion "ray" tried the fraction lost by decay was calculated.

(b) This fraction was weighted by the probability of production as a function of energy and angle of production.

(c) Rays were taken to originate in several locations in the target, each having weighting factors determined by the beam profiles and the target volume that it represented,

(d) The energy acceptance of the counter was considered.

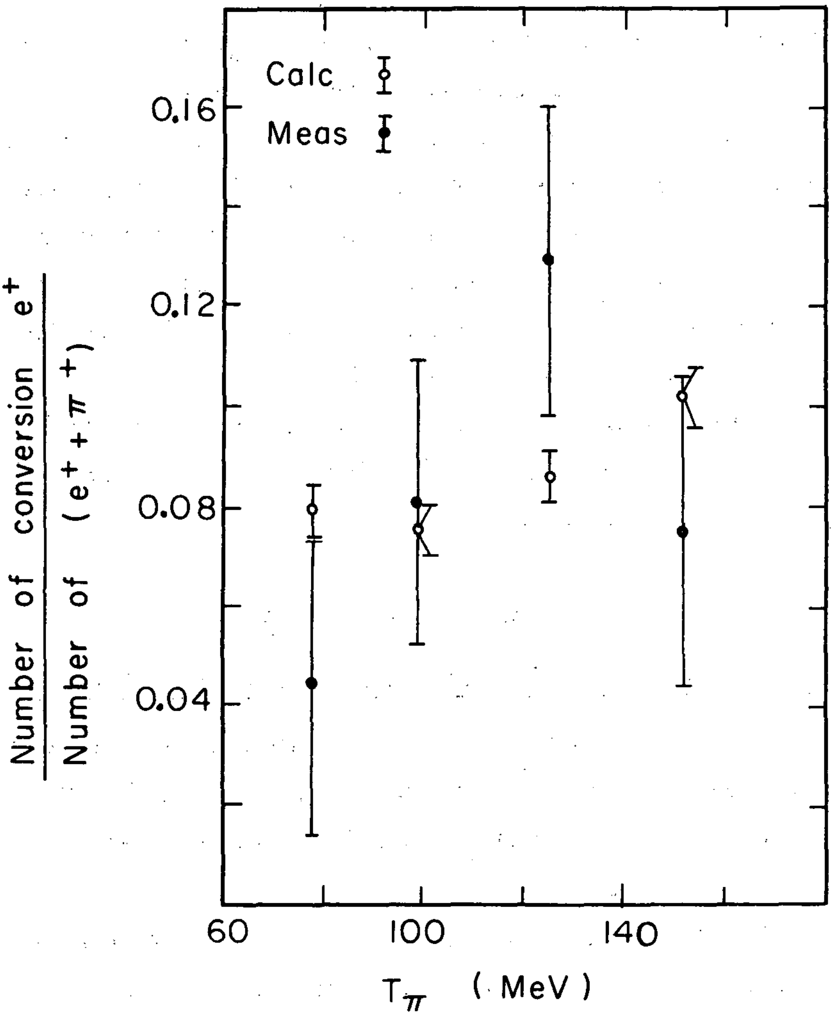

MU-29651

Fig. 14. Comparison of measured and calculated e$^+$ contamination due to γ conversion for all ππ' counters at 20° (lab) for 365 MeV incident energy.

(e) The loss was averaged over the directions, energies, and origins of all rays that could possibly enter the π counter. (Details of the calculation may be found in Appendix A.) Since the path in the spectrometer was so important for this calculation, a correction was applied for imperfections in the spectrometer-simulation process.

Every π counter lost some counts owing to pion decay, but also gained back some counts owing to the detection of muons. The muons referred to as "the gains," which were detected in a $\pi\pi'$ counter centered about π energy T_π, may have come from three sources.

Source 1. Some fraction of the muons from the decay of the original pions having energy T_π passed through the T_π counter.

Source 2. Pions having energy different from T_π and decaying in the spectrometer produced muons that may have passed through the T_π counter.

Source 3. Some pions that originally would not have passed through counters C1 and C2 decayed in such a way that some of the muons thereby produced successfully traversed the spectrometer and passed through the π counters.

The bulk of the muons--70 to 75% of the total number of muons detected--came from Source 1. Source 2 usually contributed 20 to 25% of the total "gains," while Source 3 gave only 1 to 2%. Most of the Source 2 muons were from the decay of pions having higher momentum than P_π. Only about 25% of the muons arising from the decay of a pion of momentum p_π have lab momentum $\geqslant p_\pi$.

Because different counter arrangements were used at different laboratory-system angles, the "gains" calculations, requiring a very long IBM 7090 computer program, were computed for a point target, and for a set of representative counters, not the actual ones. In order to make the gain and loss calculations compatible, the losses were also calculated for the point target, and the ratio of loss to gain for the point target was assumed to be equal to the ratio of loss to gain for the actual system. The ratio averaged over all cases was 1.7.

The correction to the π^+-detection efficiency of a particular $\pi\pi'$ counter was given by the fraction A/B. A was the net number of π^+ lost, which was equal to the difference between the number of π^+

(headed for that counter) that had decayed and the number of μ^+ detected by the counter. B was the original number of π^+ produced at the target that would have been detected by the counter (neglecting any possible decay). The correction, therefore, was the net fractional loss of π^+-detection efficiency due to decay. Because at higher lab angles the energy of the π^+ is relatively low and also because there is no large range of energies higher than the ones we measured, the gains from Sources 1 and 2 are relatively less than those gains at lower angles. The correction as calculated in Appendix A, therefore, turned out to be mostly a function of laboratory-system angle rather than of π^+ energy. The corrections are listed in Table VI.

The same corrections were applied to the 432-MeV and 365-MeV data although the gain-to-loss ratios were calculated at 365 MeV. A case was run at 432 MeV and the indications were that the corrections would be the same at the higher energy. (For details of the calculation see Appendix A.)

Table VI. Correction, as a function of angle (lab), to the π^+-detection efficiency necessitated by π^+ decay to $\mu^+ + \nu$.

Magnetic field (gauss)	Angle (lab) (deg)	% Correction
19,500	20	4.0 ± 1.0
	50	5.5 ± 1.0
15,000	80	8.5 ± 1.5
	110	9.0 ± 1.5

2. Nuclear Absorption and Multiple Coulomb Scattering

Losses due to nuclear absorption of the π^+ in the telescope and hydrogen target were calculated by using Stork's data.[17] The copper sheets placed between the π and π' counters in the high-energy channels in order to stop protons produced an average loss of 2% in the π^+.

The total absorption, including the Cu, averaged 6% for energies above 80 MeV and from 2 to 4% for energies below 80 MeV. The uncertainty assigned to the absorption correction was taken as 10% of the correction.

Losses in the telescope due to multiple Coulomb scattering were calculated by using the Sternheimer formalism[18] adapted to a rectangular geometry. The calculation was performed for Coulomb scattering in only the vertical direction, for it was assumed that each particle scattering left or right in the target and missing the telescope was compensated for by a second particle that was not headed for the telescope but was scattered into it. Also, the same effect was assumed to hold for particles scattered by counters C1 and C2 and supposed to count in the $\pi\pi'$ counters. Since the π and π' counters were only 1 inch apart, the losses due to multiple scattering in passing from the π to the π' counter were negligible.

The correction was found to be essentially zero in all cases except when data were taken with the Cerenkov counter in place. There the correction was 1.5% in the lowest energy channel (30 MeV) and zero in all others.

VI. RESULTS

A. Differential Distributions

The value of the laboratory-system differential distribution, $d^2\sigma/dTd\Omega$, was computed by

$$\frac{d^2\sigma}{dTd\Omega} = \left[\frac{Y}{nt(1-\epsilon)(\Delta T\Delta\Omega)} - \left(\frac{d^2\sigma^c}{dTd\Omega} + \frac{d^2\sigma^d}{dTd\Omega}\right)\eta_{e^+}\right]\frac{1}{\eta_\pi}, \tag{18}$$

where Y = net yield per unit monitor,

n = average number of target particles per $\text{cm}^3 = 4.15\times10^{22}/\text{cm}^3$,

t = target thickness = 10.16 cm,

ϵ = fraction of μ^- and e^- in beam,

$\Delta T\Delta\Omega$ = energy-solid-angle acceptance of the π counter,

$\frac{d^2\sigma^c}{dTd\Omega}$ = cross section for detecting an e^+ arising from γ conversion per unit pion energy and unit solid angle,

$\frac{d^2\sigma^d}{dTd\Omega}$ = cross section for detecting a Dalitz e^+ per unit pion energy and unit solid angle,

η_{e^+} = telescope detection efficiency for positrons,

η_π = telescope detection efficiency for the π^+ (this includes nuclear absorption, μ^+-decay correction, and multiple Coulomb scattering).

The uncertainty in $d^2\sigma/dTd\Omega$ was determined from the uncertainties of the listed quantities under the assumption that these were normally distributed.

For each pion laboratory-system angle, energy, and cross section, the corresponding center-of-mass quantities T^*, θ^*, and $d^2\sigma/dT^*d\Omega^*$ were computed. Table VII is a listing of the final values for these quantities at both 365 and 432 MeV.

The most interesting feature of the measured π^+ c.m. differential distributions is the low-energy peaking of the energy spectrum. A typical spectrum, the c.m. distributions for the 50-deg laboratory-system data, $\theta^*_{\text{average}}$ = 73 deg at 365 MeV incident energy, is plotted in Fig. 15. The curve drawn is the phase-space distribution. A complete graphical presentation of the data may be found in Sec. VII. A, Figs. 18 and 19.

TABLE 7 PART 1
DIFFERENTIAL DISTRIBUTIONS

INC ENERGY MEV.	THETA DEG.	T MEV.	DT MEV.	LAB. CROSS SECTION MICROBARNS/ MEV-STER.	THETA* DEG	T* MEV.	DT* MEV.	C. OF M. CROSS SECTION MICROBARNS/ MEV-STER.	
365.0	20.0	78.3	8.2	4.02 +/- 0.31	32.7	35.6	4.6	2.55 +/- 0.20	
365.0	20.0	100.0	10.5	3.51 +/- 0.27	31.5	49.5	6.1	2.30 +/- 0.17	
365.0	20.0	125.9	10.9	2.62 +/- 0.34	30.6	66.6	6.7	1.76 +/- 0.23	
365.0	20.0	151.9	14.2	1.67 +/- 0.14	30.0	84.1	8.6	1.14 +/- 0.09	
365.0	50.0	52.9	7.1	2.95 +/- 0.22	77.9	34.4	4.4	2.31 +/- 0.18	
365.0	50.0	73.3	8.9	2.91 +/- 0.21	74.7	49.6	5.4	2.31 +/- 0.17	
365.0	50.0	98.6	11.8	2.45 +/- 0.21	72.5	69.0	6.9	1.97 +/- 0.17	
365.0	50.0	119.2	12.8	1.84 +/- 0.18	71.3	85.2	8.4	1.48 +/- 0.15	
365.0	50.0	141.3	15.8	1.02 +/- 0.09	70.5	102.7	10.3	0.83 +/- 0.07	
365.0	80.0	32.6	1.4	2.06 +/- 0.26	113.4	37.0	1.1	2.21 +/- 0.28	**
365.0	80.0	49.6	4.3	2.13 +/- 0.16	109.3	53.4	3.1	2.22 +/- 0.17	**
365.0	80.0	72.5	7.0	1.47 +/- 0.13	106.4	75.7	5.3	1.51 +/- 0.13	**
365.0	80.0	93.6	8.5	0.80 +/- 0.07	104.9	96.4	6.6	0.81 +/- 0.07	**
365.0	80.0	116.2	12.3	0.31 +/- 0.04	103.8	118.7	9.1	0.31 +/- 0.04	**
365.0	110.0	29.8	2.4	1.84 +/- 0.25	136.6	52.0	2.6	2.52 +/- 0.35	
365.0	110.0	46.8	4.3	1.64 +/- 0.15	133.8	73.3	4.3	2.13 +/- 0.20	
365.0	110.0	61.5	6.6	0.87 +/- 0.10	132.4	91.6	6.6	1.10 +/- 0.12	
365.0	110.0	77.3	8.5	0.43 +/- 0.07	131.4	111.0	8.5	0.54 +/- 0.08	
365.0	110.0	46.9	3.8	1.38 +/- 0.14	133.8	73.6	3.8	1.80 +/- 0.18	**
365.0	110.0	61.7	6.3	0.84 +/- 0.09	132.4	91.8	6.3	1.07 +/- 0.11	**
365.0	110.0	77.3	8.5	0.39 +/- 0.05	131.4	111.0	8.5	0.49 +/- 0.07	**

** DATA TAKEN WITH CERENKOV COUNTER

TABLE 7 PART 2
DIFFERENTIAL DISTRIBUTIONS

INC ENERGY MEV.	THETA DEG.	T MEV.	DT MEV.	LAB. CROSS SECTION MICROBARNS/ MEV-STER.	THETA* DEG	T* MEV.	DT* MEV.	C. OF M. CROSS SECTION MICROBARNS/ MEV-STER.
432.0	20.0	53.6	6.3	6.01 +/- 0.60	37.9	18.6	3.1	3.35 +/- 0.33
432.0	20.0	80.4	8.1	6.97 +/- 0.51	34.4	33.9	4.5	4.22 +/- 0.31
432.0	20.0	111.6	11.6	6.50 +/- 0.43	32.6	53.0	6.4	4.13 +/- 0.27
432.0	20.0	137.8	13.9	4.30 +/- 0.31	31.7	69.7	8.1	2.80 +/- 0.20
432.0	20.0	166.5	19.3	2.73 +/- 0.23	31.1	88.4	9.0	1.81 +/- 0.16
432.0	50.0	54.9	7.2	4.96 +/- 0.36	80.8	35.1	4.2	3.85 +/- 0.28
432.0	50.0	79.0	8.8	4.23 +/- 0.31	76.9	52.8	5.6	3.33 +/- 0.24
432.0	50.0	102.5	10.5	4.35 +/- 0.49	74.8	70.5	7.9	3.45 +/- 0.39
432.0	50.0	124.4	12.3	3.35 +/- 0.29	73.6	87.4	7.8	2.68 +/- 0.23
432.0	50.0	160.6	16.0	1.25 +/- 0.15	72.3	115.7	10.3	1.00 +/- 0.12
432.0	80.0	32.5	2.8	2.36 +/- 0.28	116.4	38.5	2.2	2.60 +/- 0.31
432.0	80.0	56.1	4.7	3.61 +/- 0.27	110.9	61.4	3.6	3.80 +/- 0.29
432.0	80.0	74.4	7.1	2.92 +/- 0.20	108.7	79.4	5.7	3.04 +/- 0.21
432.0	80.0	97.0	9.6	2.17 +/- 0.22	107.1	101.7	7.4	2.23 +/- 0.23
432.0	80.0	113.7	10.6	1.20 +/- 0.14	106.2	118.2	8.5	1.23 +/- 0.14
432.0	110.0	33.2	3.2	1.89 +/- 0.18	137.8	60.0	3.3	2.65 +/- 0.25
432.0	110.0	50.4	5.2	1.81 +/- 0.14	135.3	82.1	5.0	2.41 +/- 0.19
432.0	110.0	66.0	7.0	1.83 +/- 0.12	133.9	101.8	5.2	2.39 +/- 0.16
432.0	110.0	85.8	8.7	0.82 +/- 0.07	132.8	126.6	8.9	1.05 +/- 0.09
432.0	110.0	107.1	11.2	0.22 +/- 0.04	132.0	153.0	10.9	0.28 +/- 0.04

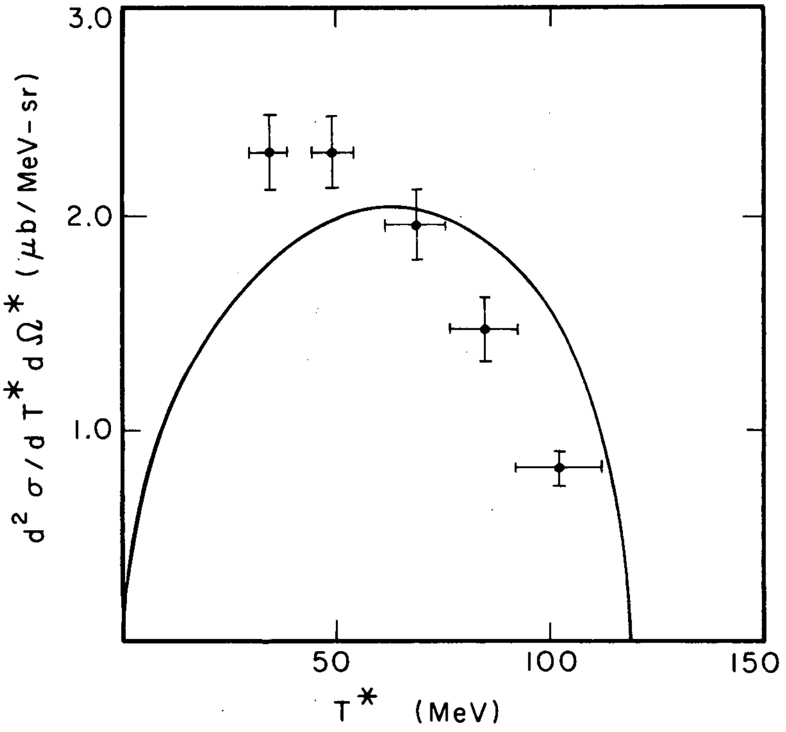

MU-29652

Fig. 15. Measurement of $d^2\sigma/dT^*d\Omega^*$ vs T^* at $\theta^*_{\text{average}} = 73°$, $\theta_{\text{lab}} = 50°$, 365 MeV.

B. Angular Distributions

Since the theories describing single π production make use of the angular distribution of the π^+ (Sec. VII), a method that was not model-dependent was used to evaluate that distribution.

The c.m. angular distribution $d\sigma/d\Omega^*$ was determined by integrating $d^2\sigma/dT^*d\Omega^*$ over T^* for a constant θ^*. Although the points were not exactly at the same θ^*, their difference from the average θ^* was well within the angular resolution of the counters. One problem encountered in performing the integration over T^* was that the low-energy ends of about half the distributions were not clearly known. In those cases the lowest-energy point had the largest value for $d^2\sigma/dT^*d\Omega^*$. Therefore, there was no absolute way of knowing where the spectrum actually peaked. The remainder of the differential distribution was usually determined very well.

Two different methods were employed for the two cases. When the peak of the distribution was clearly known the integration was performed as in Fig. 16, Case 1. The dashed curve represents the curve that was integrated to give $d\sigma/d\Omega^*$. The uncertainty in the integral was given by the uncertainties in each measurement. In the case in which the peak of the curve had not been clearly observed the integration was performed as in Case 2 of Fig. 16. The part of the curve in question is from $T = O$ to $T = A$. The lower limit of the area under that part of the curve was taken to be the area of triangle OBA. The upper limit was assumed to be the area in rectangle OABD. The value used was taken as halfway between, with an uncertainty of half the difference. This uncertainty is just the area of triangle OCD. The values of $d\sigma/d\Omega^*$ are listed in Table VIII. The average total uncertainty of $d\sigma/d\Omega^*$ at 365 MeV was about 16%, and at 432 MeV, 10%.

At both incident π^- energies $d\sigma/d\Omega^*$ appears to have the linear form $d\sigma/d\Omega^* = x_0 + x_1 \cos\theta^*$. The data, along with the best straight-line fits, are plotted in Fig. 17. The values of x_0 and x_1 are listed in Table VIII.

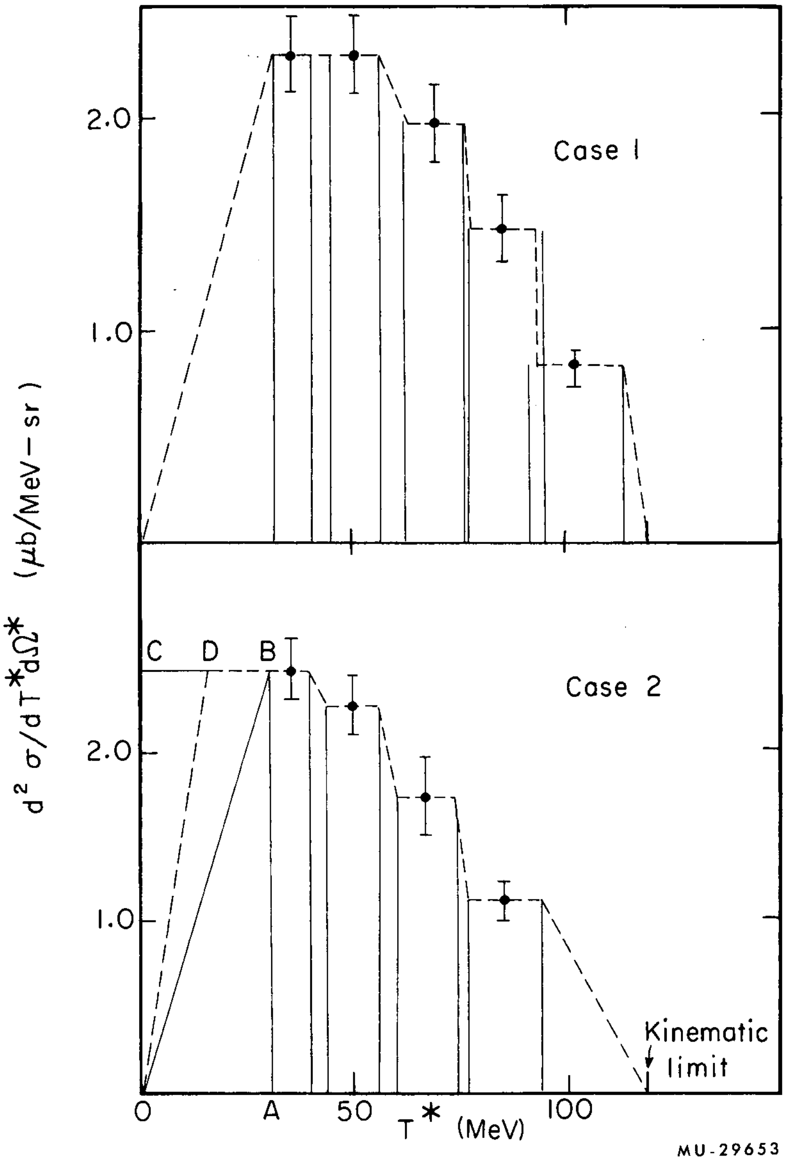

Fig. 16. Diagrams showing methods of performing T^* integration. Case 1 is at $\theta^*_{av} = 73°$, $\theta_{lab} = 50°$, 365 MeV. Case 2 is at $\theta^*_{av} = 31°$, $\theta_{lab} = 20°$, 365 MeV.

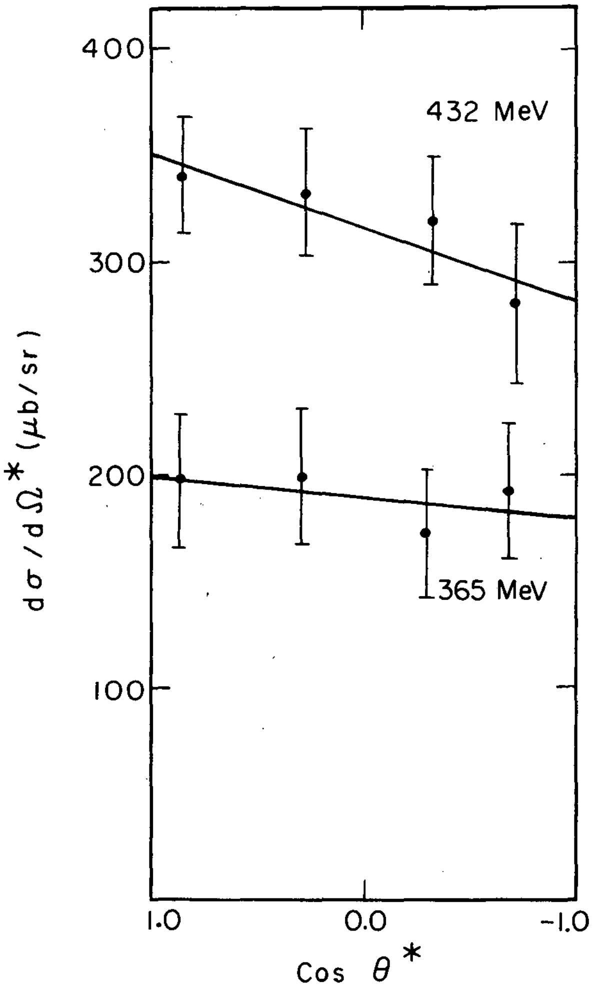

MU-29654

Fig. 17. Measured values of $d\sigma/d\Omega^*$ plotted versus cos θ^*.

Table VIII. π^+ c.m. angular distributions and their fit to the form $d\sigma/d\Omega^* = x_0 + x_1 \cos\theta^*$.

Measurements			Calculations	
T_{inc} (MeV)	$\cos\theta^*$	$d\sigma/d\Omega^*$ (μb/sr)	x_0 (μb/sr)	x_1 (μb/sr)
365	0.857	198 ± 31	190 ± 16	10 ± 27
± 15	0.292	199 ± 32		
	-0.292	172 ± 30		
	-0.682	193 ± 31		
432	0.839	341 ± 27	317 ± 16	35 ± 26
± 15	0.276	333 ± 30		
	-0.326	310 ± 30		
	-0.719	281 ± 37		

C. Total Cross Section

The total cross section was evaluated by integrating over $d\Omega^*$ the value of $d\sigma/d\Omega^*$ as given by the straight-line fits.

The values for the total cross section are

at 365 MeV, 2.39 ± 0.20 mb; and

at 432 MeV, 3.98 ± 0.20 mb.

VII. DISCUSSION

A. Kinematics

The top halves of Figs. 18 and 19 show the Dalitz plots for the reaction

$$\pi^- + p \rightarrow \pi^+ + \pi^- + n \qquad (1)$$

at 365 and 432 MeV. The ordinate is the π^- c. m. kinetic energy and the abscissa the π^+ c. m. kinetic energy. A second scale, the residual mass squared of the other two particles, is also plotted. Since only the π^+ was detected in this experiment it was not possible to determine points inside the Dalitz contour; rather, we determined the projection of the Dalitz plot onto the T_{π^+} axis. The location of the isobar, N*, is given where possible on the $(M_{\pi N})^2$ scale along with the lines representing the half-width of the isobar. Lines of constant $\omega_{\pi\pi}$ are also shown.

Let us consider how the possible type of interaction can affect the π^+ energy spectrum. An effect which is purely a function of $\omega_{\pi\pi}$ is not easily detected here because much of the π^+ energy spectrum receives contributions from the same $\omega_{\pi\pi}$. Only if there were a strong resonance at either very low or very high values of $\omega_{\pi\pi}$ would a small portion of the π^+ energy spectrum be affected. If isobar formation is the dominant interaction, then the π^+ energy region most affected is given by the projection of the isobar bands shown onto the π^+ axis. What cannot be displayed is that the formation of the isobar between the π^+ and the n and between the π^- and the n have different probabilities. Were the isobar to be formed purely between the π^+ and the n the higher π^+ energies would be favored. Were the isobar formed purely between the π^- and the n the low-energy portion of the π^+ spectrum would be favored. In actuality it is some linear combination of the two processes, including a possible interference between them. The details are discussed in VII. C.

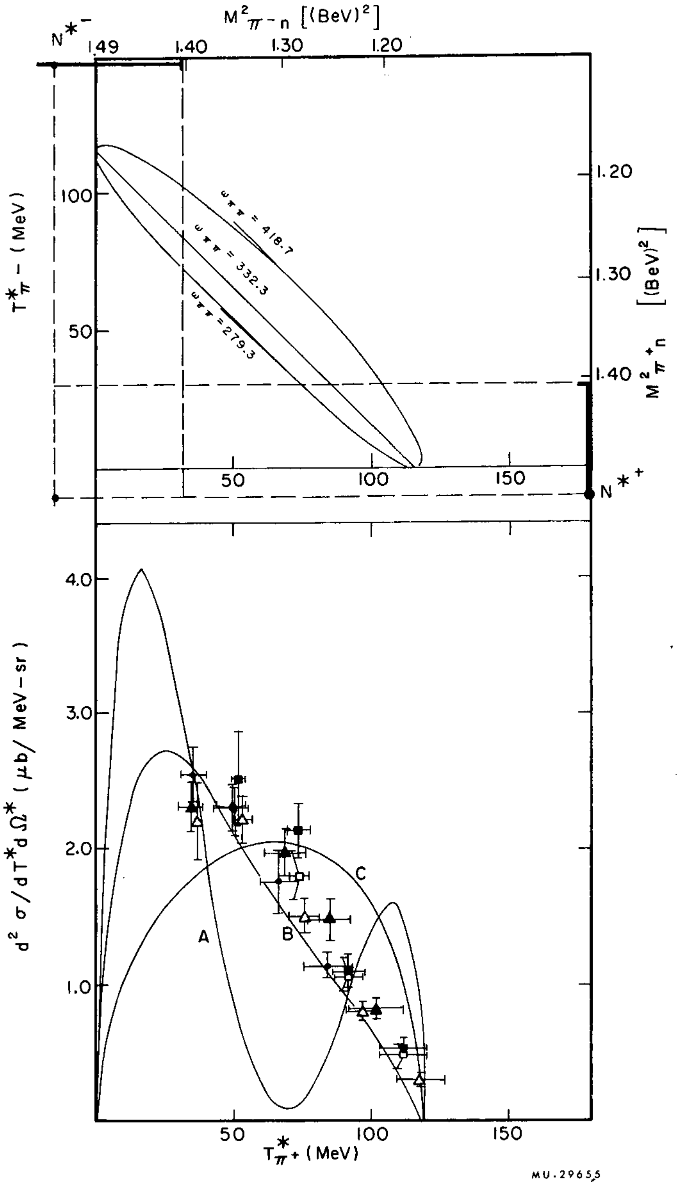

Fig. 18. Kinematics and measured $d^2\sigma/dT^*d\Omega^*$ vs T^* for 365 MeV incident energy.

● : θ^*_{av} = 31°

▲: θ^*_{av} = 73°

△: θ^*_{av} = 106° Cerenkov counter in

□: θ^*_{av} = 132° Cerenkov counter in

■: θ^*_{av} = 132° Cerenkov counter out

A = T_{init} = 3/2 s-wave isobar model

B = T_{init} = 1/2 s-wave isobar model

C = Phase space

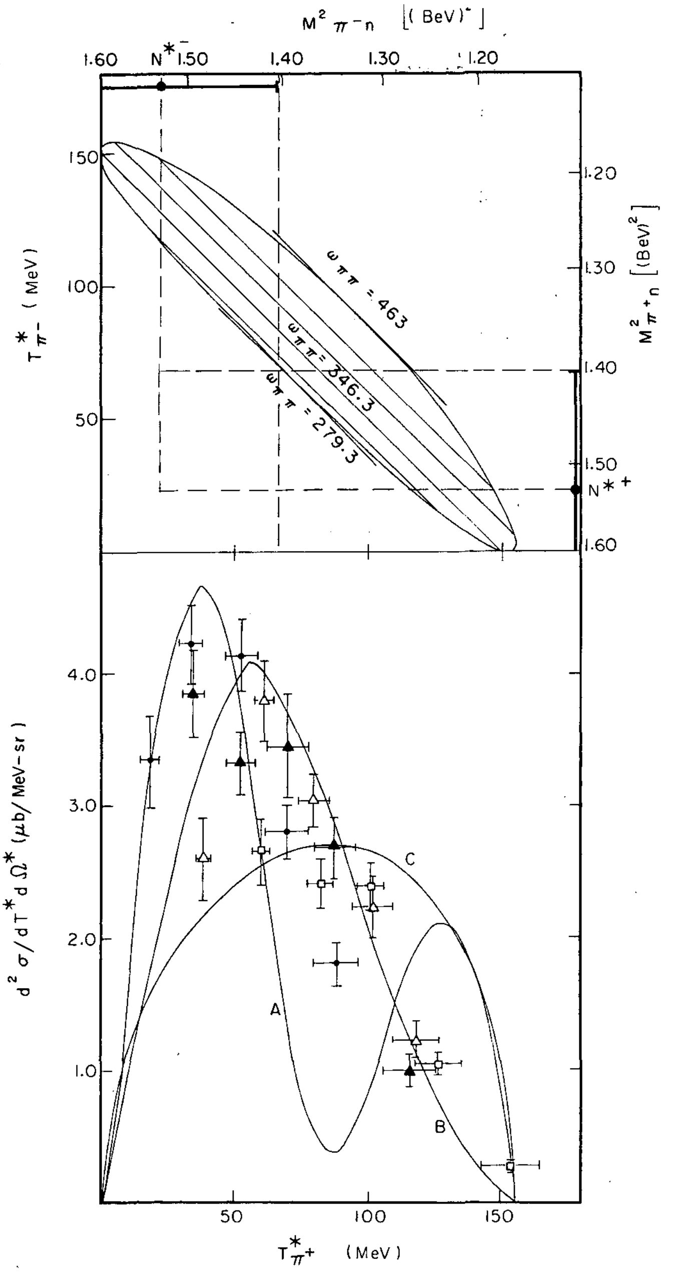

MUB-1647

Fig. 19. Kinematics and measured $d^2\sigma/dT^*d\Omega^*$ vs T^* for 432 MeV incident energy.

● : θ^*_{av} = 33°

▲: θ^*_{av} = 74°

△: θ^*_{av} = 109°

☐: θ^*_{av} = 134°

A = T_{init} = 3/2 s-wave isobar model

B = T_{init} = 1/2 s-wave isobar model

C = Phase space

B. ππ Model

The isotopic states of the final-state ππ systems for single-π production in πp reactions are given in Table IX. To satisfy Bose statistics the odd isotopic spin states require odd angular momentum states, e.g., T = 1 requires J = 1, 3, 5, ⋯, etc. Isotopic spin conservation requires that the T = 2 final ππ state be produced from the T = 3/2 initial πp state, and the T = 0 ππ state from the T = 1/2 πp state.

Table IX. Isotopic spin states for the final ππ system in πp reactions.

No.	Reaction	T
1	$\pi^- + p \rightarrow \pi^+ + \pi^- + n$	0, 1, 2
2	$\pi^- + p \rightarrow \pi^- + \pi^0 + p$	1, 2
3	$\pi^- + p \rightarrow \pi^0 + \pi^0 + n$	0, 2
4	$\pi^+ + p \rightarrow \pi^+ + \pi^+ + n$	2
5	$\pi^+ + p \rightarrow \pi^+ + \pi^0 + p$	1, 2

The analysis of single-π production according to a ππ interaction model was made most explicit by Goebel and Schnitzer (hereafter designated GS).[19] The dominant-production diagrams considered by GS are given in Fig. 20

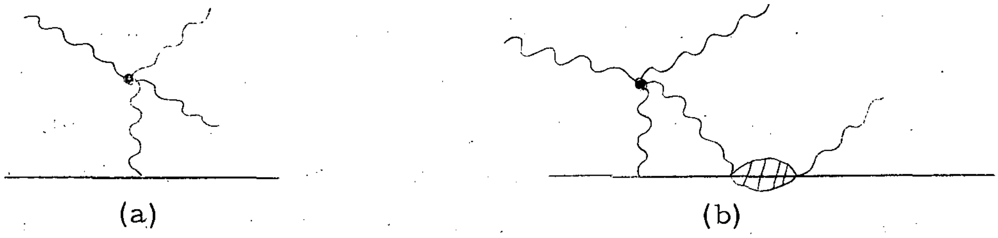
(a) (b)

Fig. 20 Dominant-production diagrams from Goebel and Schnitzer.

In Fig. 20, process (b) is the "rescattered" production, in which the rescattering is mainly in the (3, 3) state. Process (a), the "direct knock-on" production, was found to be much more important than the rescattered production.

By adding s- and p-wave $\pi\pi$ terms to the static-model formalism, GS calculated total cross sections and pion angular distributions in terms of the s- and p-wave coupling constants λ_s, λ_p. Through the total cross section, λ_s and λ_p were related to a_0, a_1, and a_2, where a_T is the scattering length for isotopic spin state T; a_0 was assumed to be 5 $a_2/2$. They then fitted their expression for the total cross section of Reaction (1) to Perkin's data and determined a set of scattering lengths. From these GS were able to predict the angular distributions and the cross sections for Reactions (1) through (5). In Reaction (1) the π^+ angular distribution was predicted to have a very strong forward and backward peaking in the c. m. system. No specific predictions were made by Schnitzer regarding the π^+ energy distributions.

Preliminary data of our measurement of Reaction (1) reported an angular distribution[20] which was not as forward or backward peaked as predicted by GS. Schnitzer therefore relaxed the $a_0 = 5\ a_2/2$ requirement and allowed all the scattering lengths to be independent parameters.[21] He used the preliminary angular distribution data at 432 MeV,[20] along with a measurement of the total cross section of Reaction (4),[22] to determine two new sets of scattering lengths (Table X). Both these sets fitted equally well the preliminary angular distribution data at 365 MeV. Both sets showed a dominance of the T = 0 $\pi\pi$ interaction. The difference between the two lay mainly in the sign of a_2.

The final results of this experiment have the same qualitative behavior as the preliminary data except that the magnitude of the cross sections is about 15% higher than previously reported. The inclusion of systematic errors in the beam monitor correction and $\Delta T \Delta \Omega$ evaluation, and a more exact treatment of the μ^+ contamination (Sec. V. C. 1 and Appendix A) are mainly responsible for this shift.

Table X. ππ scattering lengths (in λ_π) according to Schnitzer (from reference 21).

	Set I	Set II
a_0	0.50	0.65
a_1	0.07	0.07
a_2	0.16	-0.14

Schnitzer arbitrarily chose Set I of Table X with which to make predictions about Reactions (1) through (5). He found that single-π production was mainly via the initial states $(T = 1/2, D_{3/2})$, $(T = 1/2, P_{1/2})$, and $(T = 1/2, S_{1/2})$. He gives the production cross section for these and the corresponding T = 3/2 states.

Recent experimental developments and how they agree with Schnitzer's predictions based on the preliminary data can be summarized as follows.

1. The measured π^+ angular distributions of the reaction $\pi^- + p \rightarrow \pi^+ + \pi^- + n$ are plotted in Fig. 21. The curves as predicted by Schnitzer's two sets are also shown. The almost isotropic behavior of the angular distribution is present in Schnitzer's two curves, but the absolute magnitude is too low to fit the final data.

2. The measured total cross section for $\pi^- + p \rightarrow \pi^+ + \pi^- + n$ as a function of π^- incident energy is given in Fig. 22. Schnitzer's predicted curve falls just below most of the measurements; however, the sharp rise of the cross section as a function of energy is present in the prediction.

3. The total-cross-section measurement of $\pi^- + p \rightarrow \pi^- + \pi^0 + p$ at 377 MeV made by our group at the Lawrence Radiation Laboratory is in excellent agreement with the predicted value of 0.37 mb.[23] (See Fig. 23.)

4. The cross section for $\pi^- + p \rightarrow \pi^0 + \pi^0 + n$ was also measured by our group and found to be about two to three times that predicted by Schnitzer.[24] The behavior of the total cross section as a function of

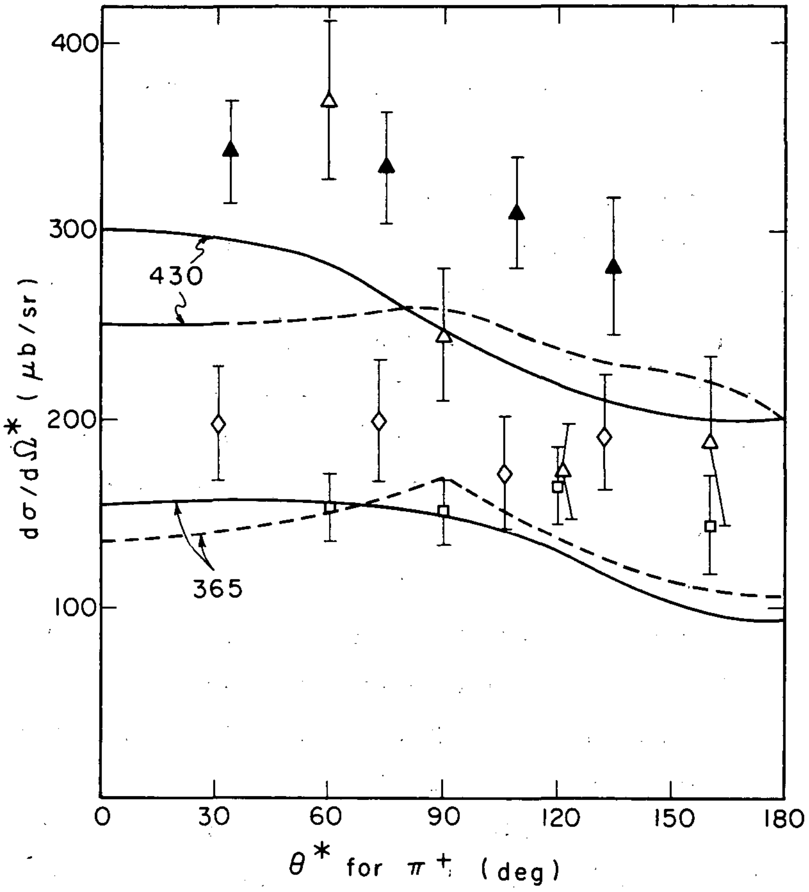

MU-29657

Fig. 21. Plot of measured π^+ angular distributions (c.m.) and Schnitzer's predictions.

□ Perkins et al. (371 MeV)
△ Perkins et al. (427 MeV)
◇ This experiment (365 MeV)
▲ This experiment (432 MeV)
— Schnitzer - Set I scattering lengths, 365 and 432 MeV.
--- Schnitzer - Set II scattering lengths, 365 and 432 MeV.

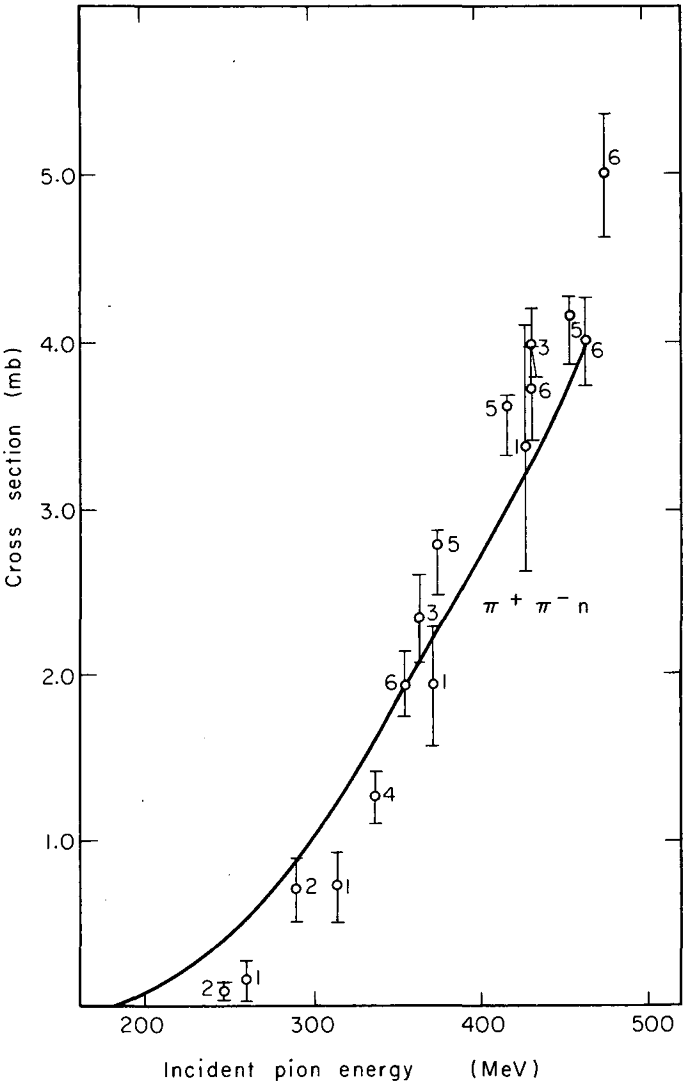

MU-29658

Fig. 22. Total cross section for the reaction $\pi^- + p \rightarrow \pi^+ + \pi^- + n$ as a function of energy.

1 - Perkins et al., ref. 4
2 - Batusov et al., ref. 36
3 - This experiment
4 - Blokhintseva et al., ref. 38
5 - Kurz, ref. 24
6 - Kirz et al., ref. 34

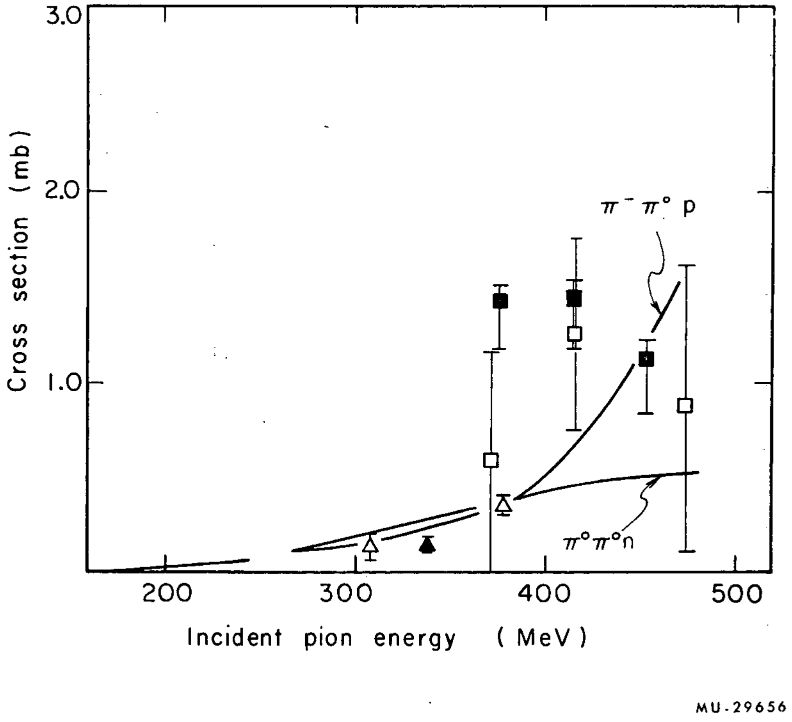

Fig. 23. Total cross section for the reactions $\pi^- + p \rightarrow \pi^- + \pi^0 + p$ and $\pi^- + p \rightarrow \pi^0 + \pi^0 + n$ as a function of energy.

△ - Barish, ref. 23.
☐ - Turley, ref. 37
▲ - Blokhintseva et al., ref. 38
■ - Kurz, ref. 24

energy, however, is somewhat like Schnitzer's predictions in that it levels off above 350 MeV. We measure essentially the same value for the cross section (about 1.45 mb) at both 374 and 417 MeV. (See Fig.23.)

5. Kirz et al., using a Chew-Low extrapolation procedure in the measurement of $\pi^+ + p \rightarrow \pi^+ + \pi^+ + n$ at 357 MeV, determined $a_2 \leqslant 0.14\ \lambda_\pi$.[25]

6. Abashian, Booth, and Crowe (ABC), in the study of pd collisions,[26] found a bump at $\omega_{\pi\pi} = 310$ MeV which could be explained by a $T = 0$ $\pi\pi$ resonance below threshold. The a_0 scattering length required to fit the ABC data is from 1 to 3 λ_π.[27]

7. Khuri and Treiman, in the analysis of the pion energy spectrum from τ decay, require an s-wave $\pi\pi$ interaction to explain the anisotropy observed. They derive the relationship $a_2 - a_0 \approx 0.7$.[28] Schnitzer's values are not consistent with this expression.

The π^+ energy distributions observed in this experiment are peaked toward lower c. m. energies. Although GS do not make any predictions of the π^+ energy spectrum, there is nothing in their model that would call for low-energy peaking. Rodberg's model requiring a strong p-wave $\pi\pi$ resonance is in contradiction to the measured distribution.

C. Isobaric Model

1. s-Wave Isobaric Model

This section contains, first, an analysis of the π^+ c. m. energy spectrum according to one isobaric model, then a discussion of the π^+ angular distribution and of the total cross section of this and other single-π-production reactions according to a second isobaric model. Since the first model lends itself to analysis of the raw data, whereas the second applies to the data only after integration over the π^+ c. m. energy, the two models are treated separately.

The qualitative aspects of the π^+ angular distribution and total cross section are in reasonable agreement with the $\pi\pi$ model of Goebel and Schnitzer, but the model does not lead to an expectation of the low-energy peaking observed here. Such a peaking would more likely be explained by an isobaric model.

Ideally the isobar N^* is an unstable particle of mass 1238 MeV having a width equal to the (3, 3) resonance. Figures 24(a) and 24(b) show the two contributing processes present in single-π production considered by the isobaric model. The model assumes that the isobar products do not interact with the recoil pion. Such a higher-order term is shown in Fig. 24(c).

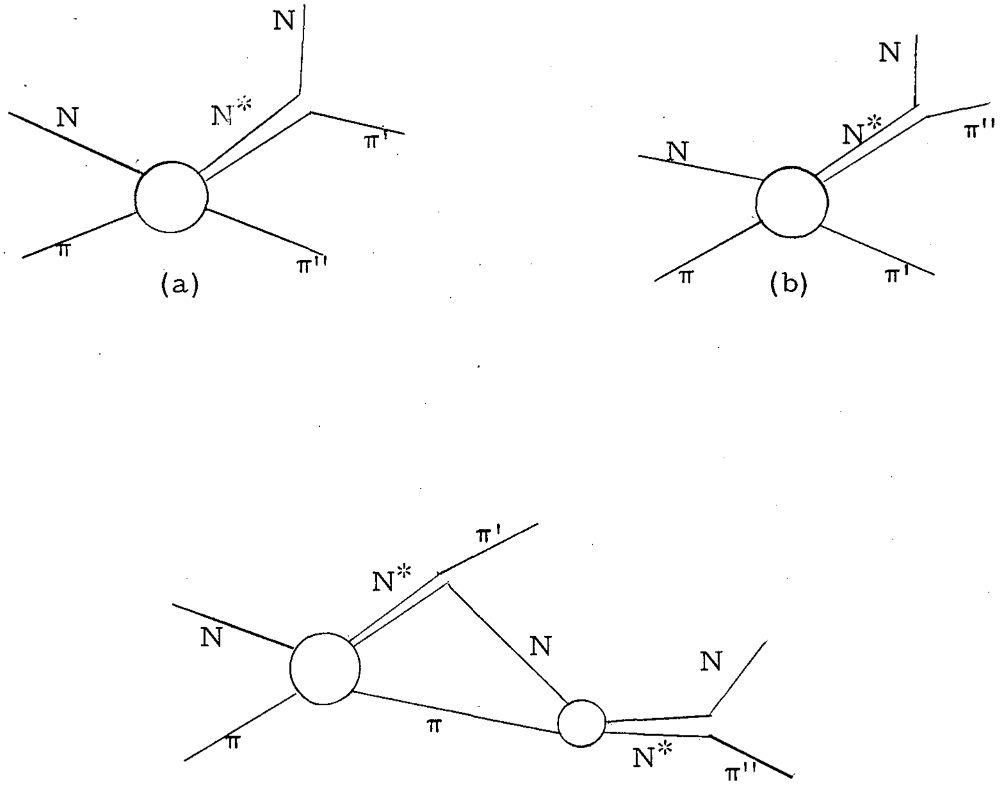

(a) (b)

(c)

Fig. 24. (a) and (b) are diagrams corresponding to two channels of single-π production according to the isobaric model.

(c) is one of many higher-order terms neglected by the isobaric model.

The model states that the isobar N^* will be produced with either of the final pions resonating with the nucleon. The probability of production is a function of the energy available to the πN system, the dependence in that system being given by the (3, 3) resonance shape.

The π and the nucleon must be in a T = 3/2 and J = 3/2 state with respect to each other. Table XI lists the isotopic spin probabilities (Clebsch-Gordan coefficients), α, that the π^+ or π^- of Reaction (1) is a member of the isobar, and β, the probability that either π is the particle that recoils opposite to the isobar in the overall center of mass. The α and β are functions of the initial-state isotopic spin. The π^+ has β greater than α for both $T_{init} = 1/2$ and $T_{init} = 3/2$.

Table XI. Isotopic spin probabilities α, β for pions in reaction $\pi^- + p \rightarrow \pi^+ + \pi^- + n$

T_{init}	Particle	Amplitude α of isobar member	Amplitude β of recoil pion
T = 1/2	π^+	$\sqrt{1/18}$	$\sqrt{1/2}$
= 1/2	π^-	$\sqrt{1/2}$	$\sqrt{1/18}$
= 3/2	π^+	$\sqrt{8/45}$	$-\sqrt{2/5}$
= 3/2	π^-	$-\sqrt{2/5}$	$\sqrt{8/45}$

An attempt was made to fit the energy spectrum observed in this experiment to an isobaric model according to Bergia, Bonsignori, and Stanghellini (designated hereafter as BBS).[29] The BBS model is an extension of the isobaric model proposed by Lindenbaum and Sternheimer (designated LS).[30]

In the LS model the observed energy spectrum of a pion in the $\pi\pi N$ final state is the sum of two spectra. The first spectrum is the result of the decay of the (3, 3) isobar into a pion and a nucleon and the second is the spectrum of the pion recoiling from the isobar. This model was applied to $\pi N \rightarrow \pi\pi N$ reactions in the region of 1 BeV with some success.[31] BBS argued that the concept of two incoherent spectra summing to give the total spectrum was not exact. Using the T-matrix formulation for the solution of the (3, 3) resonance, BBS proposed, for the T matrix in single-π production, the form

$$T_{prod} = \alpha A + \beta B, \tag{21}$$

where

α = Clebsch-Gordan coefficient (that is, probability that π' is a member of the isobar) (see Fig. 20),

A = term giving the (3, 3) resonance amplitude as a function of the total energy of the $(\pi' + N)$ system,

β = Clebsch-Gordan coefficient (probability that π'' is a member of the isobar),

B = (3, 3) resonance amplitude as a function of the energy in the $(\pi'' + N)$ system.

The cross section $d\sigma \propto |T|^2$, hence there exist interference terms. At high energies the BBS and LS spectra are somewhat similar, but at low energies (600 MeV or less) the interference terms make a great difference. Both BBS and LS calculate the π energy spectra assuming the isobar is produced isotropically (s-wave production) and decays isotropically in its own center of mass.

The validity of the BBS model depends upon the assumption that the (3, 3) resonance is the dominant resonance in the region. Because at our energies the isobar is not fully excited ($\omega_{\pi N} < 1240$ MeV) we need not worry about the higher πN resonances, but there may be $\pi\pi$ effects. One complication to the analysis of this reaction according to the isobaric model is that in the initial state both T = 1/2 and T = 3/2 isotopic spin states are present. The π^+ energy spectrum due to the different initial isotopic spin states is different, since α and β are different for the two cases.

2. Angular Momentum Analysis and p-Wave Model

Table XII gives the angular momentum analysis for the production of the isobar. The notation used is

ℓ_1 = orbital angular momentum of one final state π with respect to the nucleon in their own c.m.,

j = total angular momentum in that πN system,

ℓ_2 = angular momentum of the second π with respect to the c.m. of the πN system,

L = orbital angular momentum of π with respect to the nucleon in the initial state,

J = total angular momentum of the πN initial state.

Given in Table XII are the final configurations ($\ell_1 j \ell_2$) and the initial states L_J from which these may be reached.

Table XII. Angular-momentum analysis of T = 3/2, J = 3/2 isobar production.

Final configuration ($\ell_1 j \ell_2$)	Initial state L_J
(p 3/2 s)	$D_{3/2}$
(p 3/2 p)	$P_{1/2}$, $P_{3/2}$, $F_{5/2}$
(p 3/2 d)	$S_{1/2}$, $D_{3/2}$, $D_{5/2}$, $G_{7/2}$

Because the distribution of the π^+ at 432 MeV is not isotropic, but has a $\cos\theta^*$ dependence, I conjectured that this dependence may be due to some p-wave production of the isobar. From Table XII we see that s-wave production of the isobar may proceed only from the $D_{3/2}$ initial state. On the other hand, p-wave production may proceed from initial p states. Since the presence of D waves has been noted in this energy region,[32] it is conceivable that angular momentum states as high as D states may contribute to isobar formation in $\pi^- p \to \pi\pi N$.

I inserted a term of the form $a + b \cos\theta_{N^*}$ into the T matrix, where θ_{N^*} = c.m. angle of the isobar. As BBS and LS did, I assumed that the isobar decayed isotropically in its own center of mass. This is equivalent to the isobar's having no preferred orientation. At present there are no data on the actual polarization of the isobar and we make no attempt to consider it.

3. Fit to measured values of $d^2\sigma/dT^* d\Omega^*$

An IBM-7090 FORTRAN computer program was written to calculate $d^2\sigma/dT^*d\Omega^*$ as predicted by the isobar model for both $T_{init} = 1/2$ and $T_{init} = 3/2$ states and for both s- and p-wave isobar production. It also calculated a phase-space distribution. It then fitted the π^+ data to various linear combinations of all these, including possible interferences. Since the low-energy peaking implied that the isobar was important here (Figs. 18 and 19) the object was to try to determine just how much of the total reaction was due to the isobar formation. See Appendix B for details of the calculation.

The bottom halves of Figs. 18 and 19 show the data along with the s-wave isobar distributions and the phase-space distribution. The curves are normalized to the value of $d\sigma/d\Omega^*$ quoted in Section VI. B. Curve A is the prediction of the $T_{init} = 3/2$ s-wave isobar model. Curve B gives the $T_{init} = 1/2$ s-wave isobar model, and C is the phase-space distribution.

The relative importance of the decay, recoil, and interference terms is given by the coefficients α^2, β^2, and $2\alpha\beta$ weighted by the appropriate isobar kinematical factors. For $T_{init} = 1/2$ the recoil coefficient, α^2, is relatively more important than α^2 for $T_{init} = 3/2$. The kinematical factors for the decay and interference terms increase in relative importance as the π^- incident energy increases, since the overlap of the two isobar bands moves closer to the allowed kinematical region with higher incident energy (Figs. 18 and 19). The decay and interference terms dominate the high end of the π^+ energy spectrum and average about 30 or 50% of the intermediate-energy distribution for $T_{init} = 1/2$ or $T_{init} = 3/2$. The low end of the energy spectrum is completely dominated by recoil terms (80 to 90%). We see for both $T_{init} = 1/2$ and $3/2$ that more than half of the calculated π^+ distributions lies in the lowest third of the π^+ energy range. For the former the decay and interference terms are about 25% of the total calculated distribution, and for the latter about 50% of the total.

In Figure 18 (365 MeV) the energy distributions measured at all the various c. m. angles are plotted. Only curve B, the $T_{init} = 1/2$ s-wave isobar model, seems to have the correct shape to fit the data. At 432 MeV (Fig. 19) the energy spectrum at each c. m. angle is peaked toward low energies, but the position of the peak seems to shift with c. m. angle. At $\theta^*_{av} = 109$ deg curve B comes closest to fitting the data, but at the other angles the resemblance to the measured spectrum is poor. This was the reason the p-wave isobar model was introduced.

The fitting procedure considered each value of $d^2\sigma/dT^*d\Omega^*$ as an independent piece of information. The fit was carried out to include all the data points. No attempt was made to fit each c. m. angle separately because the energy spectrum was not determined well enough to warrant that type of analysis.

The results of fitting the data are given in Table XVII of Appendix B. The total cross section determined by the best-fit parameters is also shown. When I attempted to fit the data to just one model, either $T_{init} = 1/2$ s-wave isobar, $T_{init} = 3/2$ s-wave isobar, or a phase-space distribution, the $T_{init} = 1/2$ s-wave isobar was by far the best, but the fit still was not good. The p-wave model did not appreciably improve the fit over the s-wave model. The coefficient of the cos $\theta_N{}^*$ term turned out to be small in all cases. In attempts to fit linear combinations of the models, reasonable fits were achieved only at 365 MeV. Two combinations were modestly successful: a $T_{init} = 1/2$ s-wave isobar model with an interfering nonresonant phase-space background, and the same for the $T_{init} = 3/2$ isobar. The main difference is that in the first case the amplitudes of the isobar and phase-space background were 1.55 and 0.30, respectively, while for $T_{init} = 3/2$ the amplitudes were 0.68 and 1.05.

The 432-MeV data were not fitted well by any of the linear combinations tried, although again the best of the fits were the s-wave isobar models with an interfering phase-space background. The background increased slightly over the 365-MeV fit in the $T_{init} = 1/2$ case, but not in the $T_{init} = 3/2$ case.

The p-wave isobar model at 432 MeV gave a small negative value for the coefficient of the cos θ_{N^*} term at 432 MeV. This means the isobar has a slight preference for the backward direction (c. m.), which manifests itself in the forward peaking of the π^+. The best fits at both energies also give values for the total cross section that agree with the value (quoted in the text) obtained by integrating $d\sigma/d\Omega^*$ over $d\Omega^*$. The $T_{init} = 1/2$ isobar model gives slightly better agreement than the $T_{init} = 3/2$ model.

One thing must be noted about the fits to the data. The spread in energy and the uncertainty in the central energy of each data point are not considered in this fit. At 365 MeV in the $T_{init} = 1/2$ case more than one-half of the χ^2 is due to three of the 21 datum points.[33] Two of these are at high c. m. energies, where the energy spread of each counter is large and where the absolute magnitude of the error in the measurement is small because the cross section is small close to the kinematic limit. It is likely that a better value of χ^2 would have been achieved if the energy uncertainty and spread had been taken into consideration.

Since the $T_{init} = 1/2$ s-wave isobar model appears to have the correct energy spectrum to fit the data at 365 MeV (Fig. 18), and because the energy uncertainty and spread of the data were neglected in the calculation, it seems reasonable to say that this model is the best representation of the 365-MeV π^+ energy spectrum. If we ignore the low probability of $\chi^2 > \chi^2_{meas}$, the significant number is the ratio of the isobar to background amplitudes, which is 5.2 at 365 MeV. Although this ratio at 432 MeV is not very meaningful, since the fit to the data is not statistically strong, nevertheless its ratio is less than that for 365 MeV.

For both incident energies, 365 and 432 MeV, the peaking of the π^+ at low c. m. energy suggested the presence of the isobar (see Figs. 18 and 19). In the model used here higher-order isobar terms (Fig. 24 (c)) and other possible effects present in the reaction, such as $\pi\pi$ interactions, were not explicitly considered. The presence in this energy region of $\pi\pi$ effects in this reaction has been suggested in another of our measurements--the differential distributions of the final-state neutron[24]--and also in the recent data of Kirz, Schwartz, and Tripp.[34] The latter also saw evidence of isobar formation. At 365 MeV we were successful in fitting the data with an isobaric model in combination with a phase-space distribution, but were less successful at 432 MeV. Evidently this approximate treatment is insufficient at the higher energy. The inability to fit the π^+ spectra solely with isobar distributions is another indication of a more complex behavior.

4. Anisovich's Isobaric Model

Anisovich, using an isobaric model, makes a prediction of the total cross sections of the $\pi N \rightarrow \pi\pi N$ reactions at low energies.[6] He uses a model--not unlike the LS model--that does not consider the interference terms, but that separates the energy and angular dependences of the isobar production. He bypasses detailed consideration of the actual π energy spectra by performing an integration over energy. Anisovich does, however, consider s- and p-wave production of the isobar. He parameterizes the production in both $T = 1/2$ and $T = 3/2$ states by three amplitudes, one for s wave and two for p wave. He derives expressions for the total cross section and angular distribution of the π's in terms of these six parameters and a set of quantities which are a function only of the total energy available in the c. m. In this manner he explains the sharp rise in the total cross section as a function of energy in Reaction (1) and also the forward peaking observed by Perkins at 432 MeV.

It is possible to test the Anisovich model without knowledge of all six parameters. The total cross sections must satisfy the following two relations derived by Anisovich:

$$\sigma(\pi^+ + p \rightarrow n + \pi^+ + \pi^+) = 0.3\ \sigma(\pi^+ + p \rightarrow \pi^+ + \pi^0 + p), \qquad (22)$$

$$1.4\sigma(\pi^+ + p \rightarrow \pi^+ + \pi^+ + n) + 2\ \sigma(\pi^- + p \rightarrow \pi^0 + \pi^0 + n)$$
$$= 0.6\ (\pi^- + p \rightarrow \pi^+ + \pi^- + n) + 2.5\ \sigma(\pi^- + p \rightarrow \pi^- + \pi^0 + p). \qquad (23)$$

Since most of the experimental data available are in the region of 365 MeV, I will evaluate Eq. (23) at that energy. Some interpolation is required because the measurements were not all made at 365 MeV. At present there is no measurement available for the total cross section of the reaction $\pi^+ + p \rightarrow \pi^+ \pi^0 p$ at this energy. Therefore, Eq. (22) is not tested here. Following is a list of the reactions and the interpolated or projected cross sections.

Reaction $\pi N \rightarrow$	Measured cross section (mb)	Energy (MeV)	Projected cross section at 365 MeV (mb)
1 $(\pi^+\pi^- n)$	2.39±.20	365	2.39±.20
2 $(\pi^-\pi^0 p)$	0.37±.03	377	0.33±.05
3 $(\pi^0\pi^0 n)$	1.44±.04	374	1.25±.20
5 $(\pi^+\pi^+ n)$	0.12±.01	357	0.15±.02

With these values, Eq. (23) becomes

$$1.4(0.15) + 2(1.25) = 0.6(2.39) + 2.5(0.35)$$

$$2.71 \pm 0.40 = 2.31 \pm 0.18.$$

The total cross sections of the four reactions, therefore, seem to fulfill Anisovich's requirements.

The angular distribution of the π^+, $d\sigma/d\Omega^*$, at any one incident energy may easily be fitted by Anisovich because of the number of parameters he has available. However, he predicts that the coefficient of the $\cos\theta^*$ term, x_1, in the expansion of $d\sigma/d\Omega^*$ has the energy dependence $x_1\,(432 \text{ MeV}) \approx 2.2\, x_1\,(365 \text{ MeV})$. Our measured values are $x_1\,(432 \text{ MeV}) = 35 \pm 26$ and $x_1\,(365 \text{ MeV}) = 10 \pm 27$, yielding a ratio of 3.5 ± 9.8. The results of this test of Anisovich's theory are not meaningful, owing to the great error in the ratio. However, should the accuracy of this number by improved with later experiments, the test may be made meaningful.

D. Comment

Both the isobar model and the $\pi\pi$ model have had some success in describing the data of the single-π-production reactions at low energies. They both also have limitations. The $\pi\pi$ model does not take into account the possibility of nuclear recoil; also it uses a zero-range approximation which at high $\pi\pi$ center-of-mass energies may be a bad approximation. The isobaric models calculated so far do not take into account the decay distribution of the isobar in its own c.m., mainly owing to lack of knowledge of the isobar polarization. They also neglect higher-order terms and any possible $\pi\pi$ effects.

The energy spectrum of the π^+ in this experiment shows evidence of some isobar formation. This does not refute the $\pi\pi$ model, but suggests that the "rescattering" is larger than calculated by that model. The other piece of experimental evidence that puts the $\pi\pi$ model in jeopardy is the very high value of the total cross section for the reaction $\pi^- + p \rightarrow \pi^0 + \pi^0 + n$. Although Schnitzer's predictions were based on the preliminary data of this experiment, it does not seem reasonable that a 15% change in the $\pi^+\pi^-n$ total cross section can give him enough boost in the a_0 or a_2 scattering lengths to double or triple his $\pi^0\pi^0n$ cross-section prediction so as to agree with the experimental value.

Both models explain the sharp rise of the cross section of Reaction (1) as a function of incident energy. One attributes it to a predominance of $\pi\pi$ interaction in the $T = 0$ state and the other to the increasing probability for isobar formation.

Goebel and Schnitzer find that the initial angular momentum states $D_{3/2}$, $P_{1/2}$, and $S_{1/2}$ all contribute to the inelastic reactions, with the first two states contributing about equally and about twice as much as the third state. For the isobar model the single-π-production reactions must stem from the $D_{3/2}$ initial state at low energies (s-wave production of the isobar), but at higher energies, where p- and d-wave production of the isobar must be considered, the $P_{3/2}$, $P_{1/2}$, $F_{5/2}$, and $S_{1/2}$ states may also contribute. (See Table XII.) For the $\pi\pi$ model the dominant initial isotopic spin state is $T = 1/2$, since a $T = 0$ $\pi\pi$ combination in final state cannot be produced from a $T = 3/2$ state.

The magnitude of the total cross section for Reaction (4), which involves only the T = 3/2 initial state, indicates that the contribution of this state is small. The fit to the π^+ energy spectrum in Reaction (1) (see Table XVII) suggests for the isobar model that the T = 1/2 initial state is also dominant. The analysis according to these two models indicates that the single-π-production reactions occur mainly in the T = 1/2 state of the πp system. Also the same initial angular momentum states are emphasized. Both of these conclusions are compatible with the many proposals that inelastic reactions influence the resonances observed in the elastic scattering at 600 and 900 MeV π^- incident energy.[35]

From the experimental evidence available on the single-π-production reactions in the region of 400 MeV it appears that both $\pi\pi$ interaction and isobar formation effects are present, so that the actual production mechanism is not a simple one but is complex.

ACKNOWLEDGMENTS

I wish to express my appreciation to Professor A. Carl Helmholz and Professor Burton J. Moyer for their guidance throughout my graduate studies and research. I would also like to thank Dr. Victor Perez-Mendez for his supervision of the experimental program.

To my colleagues and friends, Dr. Barry C. Barish and Dr. Richard J. Kurz, goes a sincere thank you. They have made this work not only possible, but also enjoyable.

I am also indebted to Messers. Paul G. McManigal and Howard Goldberg for their aid in the running of the experiment, to the hydrogen target group under Edward McLaughlin for their assistance, to James Vale, the cyclotron crew, and accelerator technicians for their part in the setting up and running of the experiment, and to the scanners of the Moyer-Helmholz Group for their aid in the many tedious operations I asked them to perform.

A special thank you to Mr. Joe Good of the computing group for showing me that VARMINT wasn't so bad after all, and also for his assistance in combating that debilitating disease called "IBM fatigue."

Finally I am indebted to Miss Miriam L. Machlis for taking my illegibly scrawled manuscript and transforming it to legible type.

This work was done under the auspices of the U. S. Atomic Energy Commission.

APPENDICES

A. Calculation of π^+ Efficiency Loss due to the Decay $\pi^+ \rightarrow \mu^+ + \overline{\nu}$

1. Simulation of Spectrometer on the IBM 7090 Computer

The number of pions that decay in flight is a function of the energy of the pion and the total path traversed. In order to guarantee that the computed path length of a pion in the spectrometer be almost the same as the actual path length the computer program had to fulfill two requirements.

a. The calculated line of energy foci for a point source at the center of the target had to coincide with the experimentally measured line of foci. This line had determined the placement of the π counters. (See Sec. III.C.)

b. The entrance and exit angles for the "rays" passing through the center of C2 from the point source had to agree with the measured values.

Figure 25 gives the ideal field shape assumed in the calculation along with the shape of the actual pole pieces. X1 and X2 are parameters that determine the size of the ideal field. The only other variable is the magnitude of the field B_z. The values of the three parameters that best fit the measurements made on the spectrometer are given in Table XIII.

Table XIII

I_{mag}	Measured field	Ideal field		
		B_z	X1	X2
(A)	(gauss)	(gauss)	(in.)	(in.)
998.24	19,500	20,500	0.5	1.0
561.3	15,000	15,750	1.0	1.0

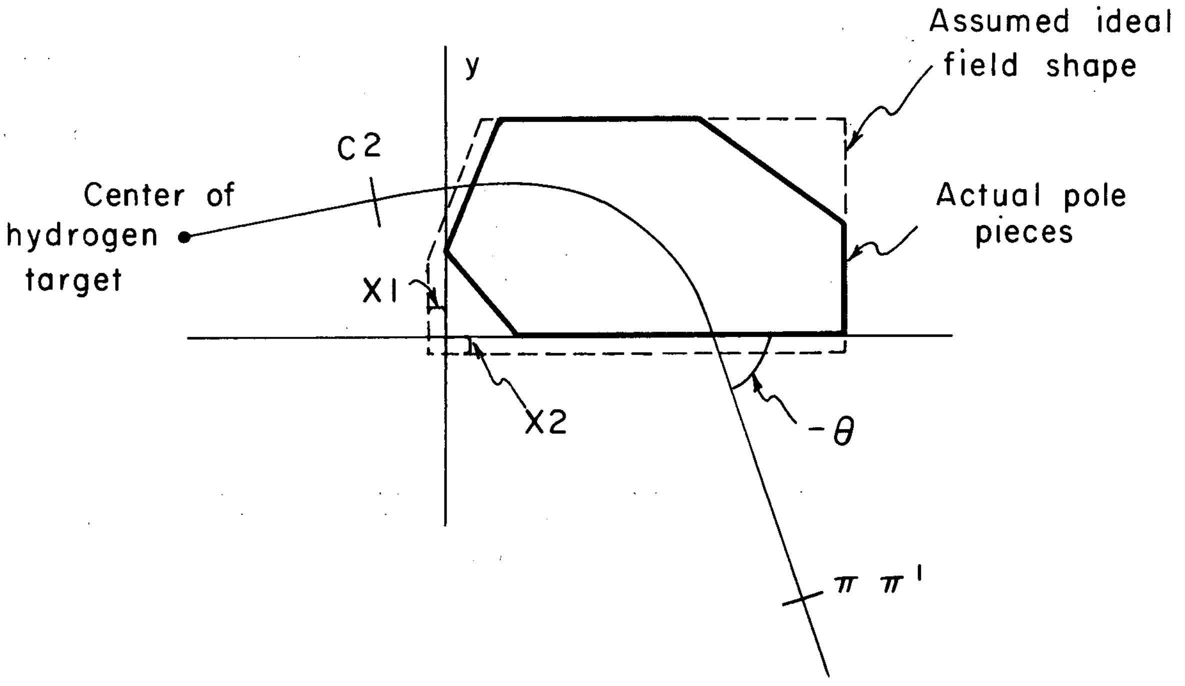

MU-29659

Fig. 25. Diagram of actual magnetic spectrometer pole pieces along with field shape assumed for efficiency-loss calculation.

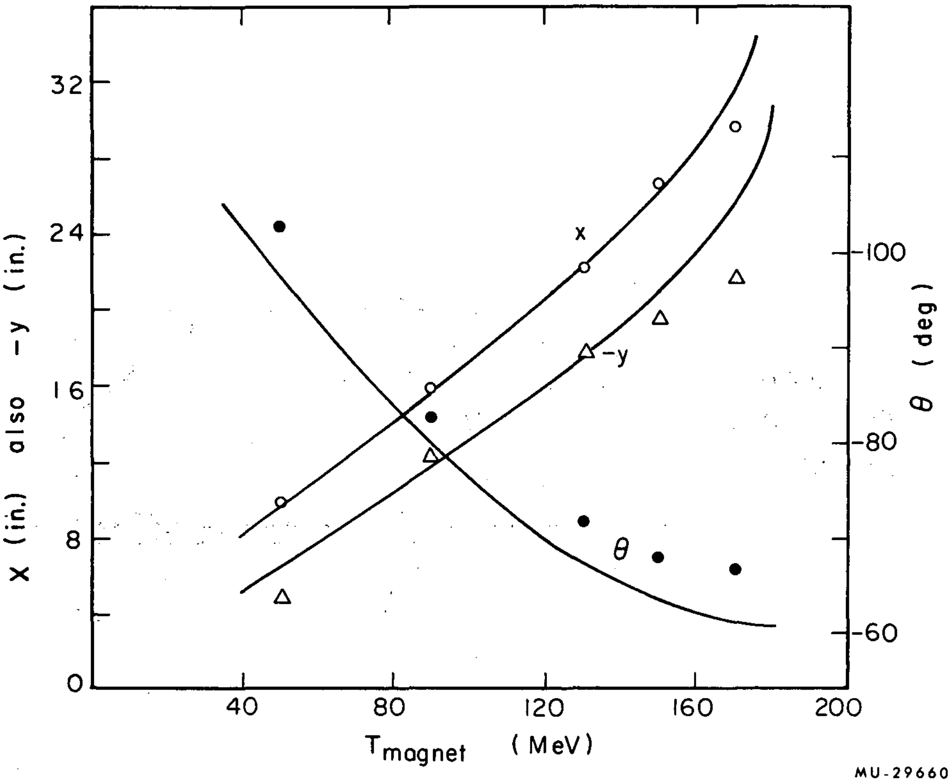

Fig. 26. Comparison of values measured on actual magnetic spectrometer with calculated values for the coordinates of the line of energy foci of a point target located at the center of the hydrogen target position.

Measurements

o : x
Δ : -y
● : θ

Figure 26 is a plot of the coordinates of the line of energy foci for a point target as a function of the pion energy in the spectrometer for the 19,500-gauss case. The coordinate system used is given in Fig. 25. The angle θ is that between central ray (a ray from the center of the target passing through the center of C2) and the x axis. The smooth curve is taken from measurements, and the points are the best calculated values. Note that the agreement is good except for the y coordinate at high energies. Since the high-energy rays emerge from the magnet almost perpendicular to the edge, $-70 \text{ deg} \geqslant \theta \geqslant -90$ deg, the difference between the computed path and actual path is almost the difference in the y values. The actual difference in path is

$$\Delta S = \left[(\Delta y \sin\theta)^2 + (\Delta x \cos\theta)^2 \right]^{1/2} \approx \Delta y, \tag{24}$$

where Δx = difference between the computed and measured values of the x coordinate of the line of energy foci,

and Δy = difference between the computed and measured values of the y coordinate of the line of energy foci.

It was then a simple matter to correct the computed path to give much better agreement with the actual path at all energies. The most probable reason for the great deviation at high energies was the simplifcation of the field shape for the computation in the region $y \geqslant 5$ and $x \geqslant 15$.

The second consideration with respect to the "computed spectrometer" was whether π counters placed at the computed energy foci had an energy-solid-angle response, $\Delta T \Delta \Omega$, that resembled the measurements described in Sec. IV.B. A simplification made in the computation was that the π and π' counters were lumped into one counter. The calculated values for counter π_2 at 50 deg, 365 MeV are plotted along with the actual measurements in Fig. 27. The computed energy acceptance width is almost the same as the actual width, but the computer favored lower-energy pions more than the actual spectrometer for any given π counter. This feature tended to slightly increase the calculated fraction lost because it weighted the lower-energy rays more than the actual spectrometer did. The inability to accurately duplicate the energy response of the π counters then meant that the calculation could be

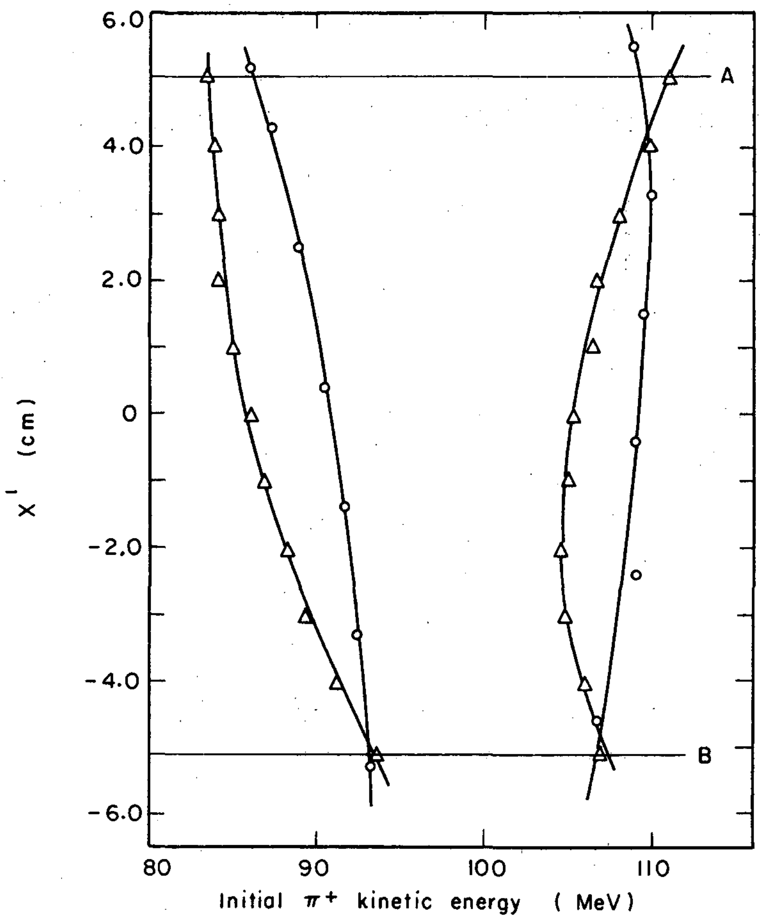

MU-29661

Fig. 27. Comparison of suspended-wire measurements with simulation on computer for counter $\pi\pi'_2$ at 50 deg for 365 MeV incident energy. Origin of rays is at target center.
o Measured
△ Simulated on computer

done only for a representative counter system. The representative system, however, would behave very much like the actual system when it came to determining which counters detect the muons lost from π rays of other energies, and even what fraction of the muons get back into the counter for which the decaying π was headed.

2. Calculation of Losses for the Actual Target

The average decaying fraction of the pions headed for a $\pi\pi'$ counter was calculated by using the formula

$$\overline{F} = \sum_{j=1}^{15} W(j) \left\{ \sum_{k=1}^{3} \left[W(k) \frac{d^2\sigma}{dT_k d\Omega}(T_k, x)\, \Delta x \left(\sum_{\phi_{\min}}^{\phi_{\max}} F_j(\phi, x, T_k)\, \Delta\phi \right) \right] \right\}. \tag{25}$$

In this equation the terms are as follows.

$W(j)$ = weight of the <u>j</u>th hydrogen target point, considering both the target volume it represents and the beam profile at the target,

x = cosine of the angle of π^+ production with respect to the incident beam,

ϕ = azimuthal angle of the π^+ with respect to incident beam,

T_k = <u>k</u>th energy value.

The energy acceptance of a π' counter as a function of energy was taken to be flat, and the limits were taken to be the measurements of the energy acceptance. These energies were slightly shifted with respect to the computed acceptance, but it turned out that the loss was a very slowly varying function of the energy, because the higher-momentum particles had longer paths than the lower-momentum particles (see Table XIV, this section.) Three energies were chosen to represent the energy acceptance of the counter. See Fig. 28. The central energy was weighted twice as heavily as the end energies.

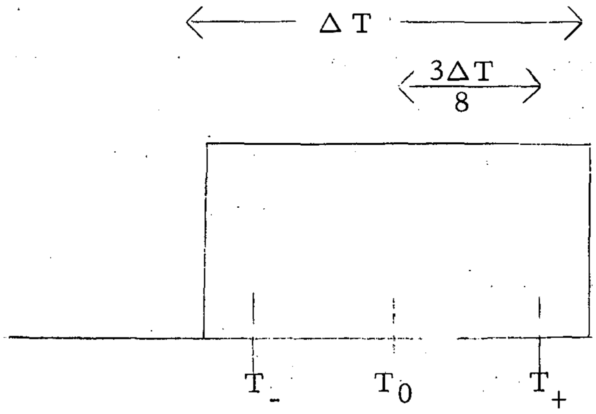

Fig. 28. ππ' counter energy acceptance as a function of energy used for the loss calculation.

W(k) = weight of kth energy value.

$\frac{d^2\sigma}{dT_k d\Omega}(T_k, x)$ = cross section for production of π^+ of energy T_k at an angle to the incident beam whose cosine is x. The preliminary values of $\frac{d^2\sigma}{dT_k d\Omega}(T, x)$ were used in this calculation.[20]

$\Delta x \Delta\phi$ = unit of solid angle (lab).

ϕ_{min}, ϕ_{max} = the limiting values of ϕ subtended by counter C2 at $\cos\theta = x$.

$F_j(x, \phi, T_k)$ = the decaying fraction of pions, with energy T_k, originating at the jth target point headed in a direction given by x, ϕ. Each pion was representative of a unit solid angle $\Delta x \Delta\phi$ centered at x, ϕ. Approximately 30 rays passed through C2 from each hydrogen target point. For each ray, the path lengths from the target to C2 and from C2 to the ππ' counters were determined. In order to take into consideration the energy losses due to ionization in the target and counters C1 and C2, the energy of the pion at the position of counter C2 was decreased in the calculation by the average ionization loss up to that point.

The fraction $F_j(x, \phi, T_k)$ was given by

$$\left\{ 1 - [\exp(-S_1/S_1')] [\exp(-S_2/S_2')] \right\} ,$$

where S_1 = path length from jth target point to C2,

S_1' = mean path for initial momentum,

S_2 = path length from C2 to ππ' counter,

S_2' = mean path for momentum of pion in magnet.

The fraction of π^+ lost, $\overline{F}$, varied very slowly as a function of energy because the lower-energy particles, although having a much smaller mean path than the high-energy pions, also had a much smaller total path length. The fraction $\overline{F}$, the total path traveled, and the central energies are listed in Table XIV for the π counter arrangement at 50 deg for 365 MeV incident π energy.

Table XIV. $\overline{F}$, average decaying fraction of π^+ for 365 MeV, 50 deg (lab).

Counter No.	Initial energy (MeV)	Total path (in.)	$\overline{F}$
π1	53	40	0.129
π2	73	44	0.127
π3	95	49	0.125
π4	117	54	0.124
π5	145	62	0.123

3. Calculation of Gains and Losses for a Point Target

a. Definition of loss and gain integrals

L, the number of pions lost to a ππ' counter, is given by

$$L = A \int_{T_{min}}^{T_{max}} \int_{\Omega_{\pi\pi'}} \sigma(T, x) \left[\int F(S, S', T) dS \right] dT d\Omega, \qquad (26)$$

where $F(S, S', T) = \dfrac{\exp[-S(T)/S'(t)]}{S'(T)}$ = probability of decay per unit path ds of a pion having kinetic energy T at a distance s along its path,

$S'(T)$ = mean path length for pion having kinetic energy T,

$\sigma(T, x) = \dfrac{d^2\sigma}{dTd\Omega}(T, x)$ = probability of production of a π^+ per unit solid angle per unit energy at angle $\cos^{-1}x$ and having energy T, (27)

$\Omega_{\pi\pi'}$ = effective solid angle subtended by counter $\pi\pi'$ with respect to the target (this usually was defined by counter C 2),

T_{min}, T_{max} = limits of the energy acceptance of the $\pi\pi'$ counter (a rectangular energy distribution was assumed),

A = factor containing the flux of incident π^- and the number of target centers per cm^2,

S_{tot} = total path length.

The number of π^+ produced per unit solid angle per MeV is given by the product $A\sigma(T, x)$. The number of π^+ decaying over the π^+ path is the integral inside the bracket of Eq. (26). The total lost to a $\pi\pi'$ counter must be integrated over the solid angle-energy acceptance of the counter.

The number gained in a counter $\pi\pi'$ is given by

$$G = A \int_{T_{KL\,min}}^{T_{KL\,max}} \int_0^{4\pi} \sigma(T, x) \left[\int_{S=0}^{S_{tot}} F(S, S', T)\, G_{\pi\pi}'(S)\, dS \right] dTd\Omega, \tag{28}$$

where $G_{\pi\pi'}(S)$ = fraction of the pions of energy T that have decayed at point S and end up in counter $\pi\pi'$.

$T_{KL\,min}$, $T_{KL\,max}$ are the kinematic limit energies.

The integration of Eq. (28) must be performed over all space and all available energies. For rays that do not pass through C2, S_{tot} is small, however, so that their contribution to G is small.

b. Integration over pion path

The integration over the path s was performed on the computer in the following way. At some point s along the path the pion was allowed to decay to a $\mu^+ + \overline{\nu}$. The decay in the pion c.m. is isotropic. The c.m. solid angle was then broken up into 400 equal sized units and a representative set of c.m. values of $\cos\theta, \phi$ were chosen to represent the unit of solid angle. The rays having these values of $\cos\theta$, ϕ were transformed into the moving π^+ coordinate system and further transformed to a coordinate system with respect to the magnetic spectrometer. Each μ was then traced until its journey ended somehow--e.g., it entered a counter or got lost in one of the pole pieces. The μ's were put into 12 different bins, six of these being π counters and six in other categories. The ratio of the number of counts in any bin to 400 was then the fraction of the π's that had decayed at point S and that ended up in that bin. For the $\pi\pi'$ bins this fraction was $G_{\pi\pi'}(S)$.

A number of points were chosen along the ray. For rays not passing through Counter C2 five points were chosen, and for those passing through C2 14 points were taken. The integral over the path was broken up into two parts, decays before and after C2. Again after C2 the energy loss was included and the pion energy decreased from its initial value by the average energy loss in the target and C1 C2 counters. The integration was performed by Simpson's rule for rays not passing through C2, and by Gaussian quadratures for rays passing through C2. All the μ's were placed in some bin and the sum of the separate integrations over the 12 bins was compared to the total fraction of pions that had decayed. These numbers were the same, therefore all μ's were accounted for.

A trial run was made using 800 rays in the π c.m. and the results agreed within 6% with those for which 400 rays were used. Also runs were made by using 12 and 17 points of decay along the paths of particles passing through C2. The results of these two agreed to 10%. Fourteen points of decay were decided upon for the final runs.

The functions $G_{\pi\pi'}(S)$ for $\pi\pi'_1$ and $\pi\pi'_2$ at 50 deg, 365 MeV are plotted in Fig. 29 for a pion of energy 53 MeV that passes through the center of C2 and $\pi\pi'$.

c. Choice of π^+ rays

The muons resulting from π decay are confined to a cone (in the laboratory system) whose axis is along the original direction of the pion and whose cone angle is given by the formula

$$\tan \theta_c = \beta/[\gamma_\pi(\beta_\pi{}^2 - \beta^2)^{1/2}] , \qquad (29)$$

where θ_c = muon cone angle (lab),
γ_π = E_π/μ:[pion energy (lab)]/[rest mass of the pion],
β_π = v_π/c = [pion velocity (lab)]/c,
β = v_μ/c = [muon velocity (in the π c. m.)]/c.

For each energy chosen the cone angle was determined and limits set on the π^+ directions to be tried. Next, representative rays were chosen within those limits. Six of these passed through C2 and 48 did not. These were all chosen in the region above the midplane of the spectrometer because the system was symmetric above and below the plane. The computer time (on the IBM 7090) required to run these 54 rays for π^+ of one energy, including all the decay μ rays, was about 35 minutes. The calculation was performed for a representative set of counters and energies at 50 and 110 deg, which have different magnetic-field settings, and the corresponding quantities calculated for a system at 30 deg less, or at 20 deg and 80 deg. It was therefore possible to do all four laboratory-system angles in two sets of runs.

d. Solid-angle and energy integration

The solid-angle integration of Eqs. (25) and (28) was done by hand. The energy integration was performed in the following way: Both losses and gains were calculated for pion energy values equal to the central energy of the representative counters. For each counter the value of the loss or gain over the whole energy acceptance of the counter was assumed to be constant. The gains, however, had contributions from

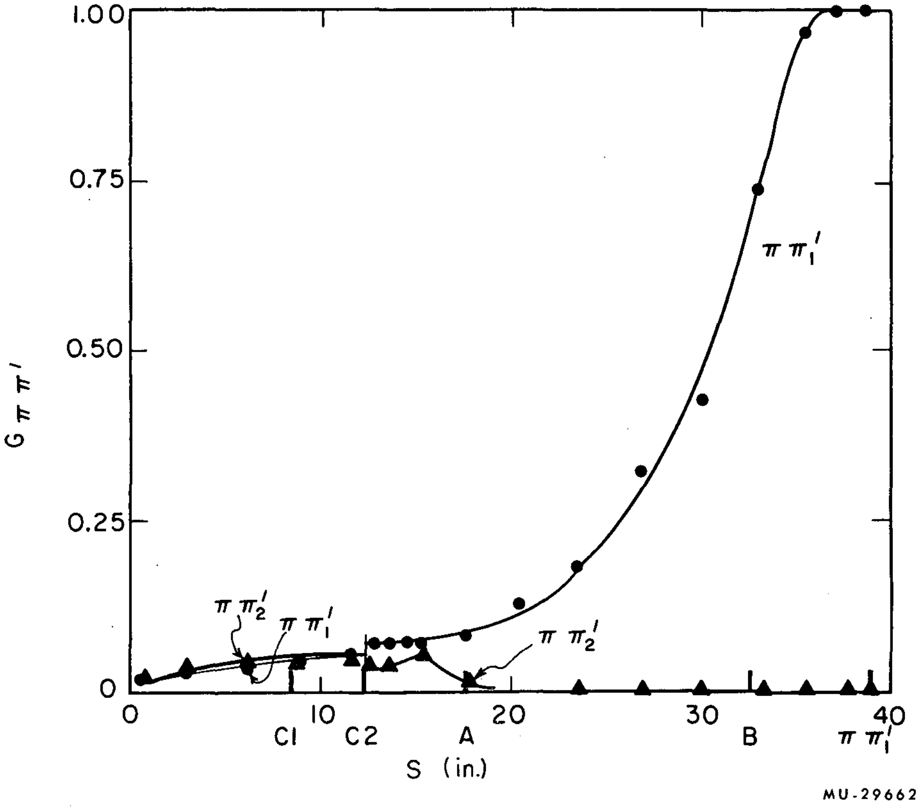

Fig. 29. $G_{\pi\pi'_1}$, $G_{\pi\pi'_2}$ plotted as a function of path traveled, s, for a 53-MeV π^+ passing through the center of C2 and counter $\pi\pi'_1$. The discontinuity at s = 12.25 is due to method of considering the loss of energy by the π^+ up to that point. See text for details.

A, B: limits of magnetic field.

C1, C2, $\pi\pi'_1$: are positions of those counters.

A point of entry to magnet.

B point of exit from magnet.

△ $G_{\pi\pi'_2}$ ○ $G_{\pi\pi'_1}$

outside energies, therefore a curve including the other energy points was drawn and added to the rectangular distribution. A sample case, the $\pi\pi'_2$ counter at 50 deg, was run, wherein the gains were calculated in finer steps of energy within the range of the acceptance of the counter. The approximation of rectangular energy response in the counter was found to be a fair one. This method was then used in all cases. The gains as a function of energy for the 50-deg counters at 365 MeV may be seen in Fig. 30. The other cases were done in a like manner.

4. Efficiency Correction Factor

The ratio of the gains to losses was calculated for the point target. It was assumed that this ratio was valid for the actual target configuration. The efficiency correction, therefore, was given in terms of gains G, loss L, and the fraction $\overline{F}$ by the equation

$$C = \left(\frac{G}{L}\right) \overline{F} . \tag{30}$$

The uncertainty in the value of C was dependent upon the uncertainties in the numbers $\overline{F}$ and (G/L). Much care was taken to get $\overline{F}$ as accurately as possible, as described in the first section of this Appendix. The fact that $\overline{F}$ was a slowly varying function of the energy was fortunate in keeping its uncertainty low (about 5%). The greatest uncertainty in C comes from the calculation of (G/L) and the assumption that (G/L) for a point target is the same as (G/L) for the whole target.

In the evaluation of G a number of uncertainties were introduced. The choice of 400 representative rays in the π^+ c.m. and 14 decay points gave a value to the integral over the π^+ path that was good to within 7%. The energy integration was crude, but it was performed in the same way for both G and L so that the ratio of G/L should not suffer much from the crudeness of the method. For the assumption that (G/L) of a point target was equal to the (G/L) for the actual target another 5% was added to the uncertartainty of (G/L).

The uncertainty assigned to the efficiency correction C averaged 20%. The calculated corrections as a function of energy are plotted

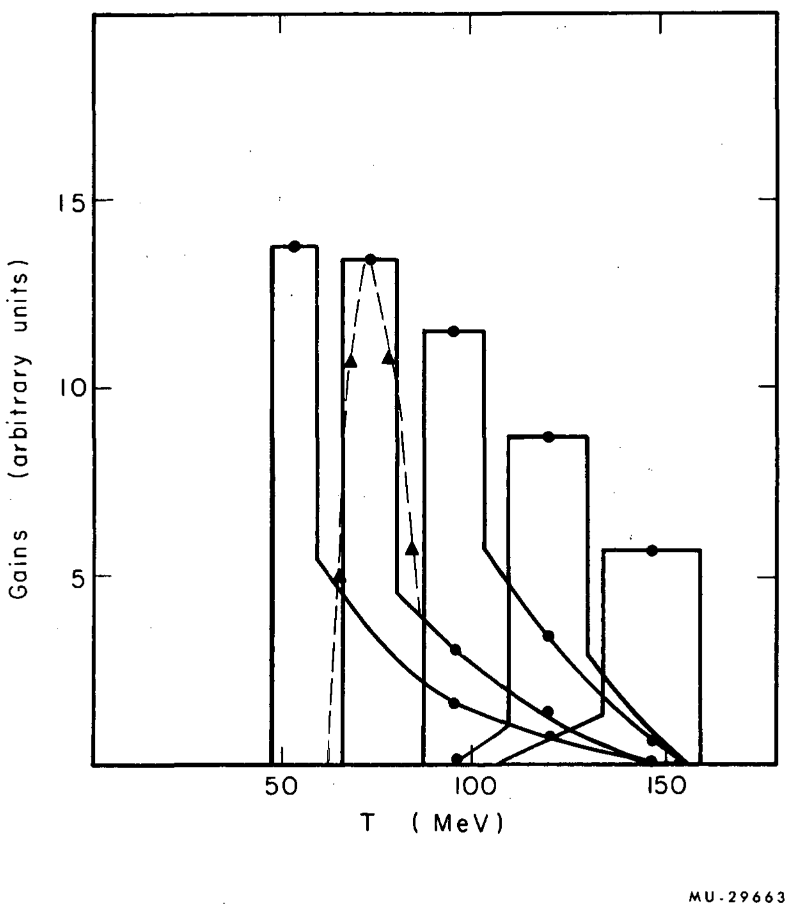

Fig. 30. Plot of G, gains, vs π^+ energy for several $\pi\pi'$ counters at 50 deg for 365 MeV incident π^- energy. The dashed curve is the calculated gains for counter $\pi\pi'_2$. The histograms with tails are the shapes used for the calculation.

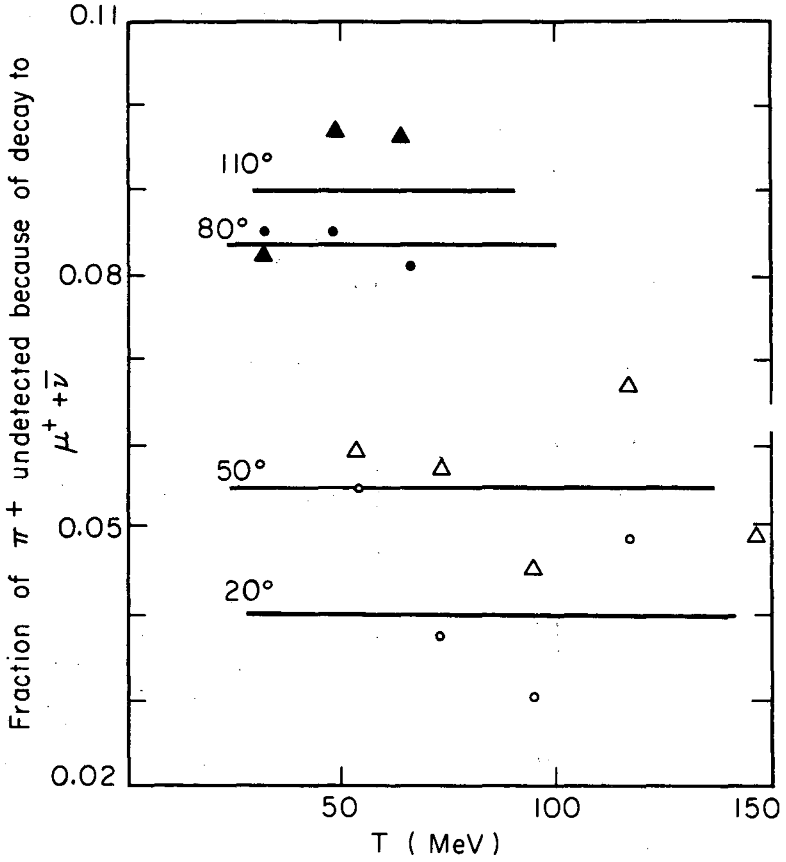

MU-29664

Fig. 31. Fraction of π's undetected because of decay to $\mu^+ + \bar{\nu}$. as a function of T_{π^+}

o $\theta = 20°$

△ $\theta = 50°$

● $\theta = 80°$

▲ $\theta = 110°$

in Fig. 31. Note that the correction is reasonably constant as a function of energy, but changes with angle. The calculation was performed for trial points at 432 MeV and found to be about the same as for the 365-MeV points. The correction applied to 432 MeV was therefore taken to be the same as at 365 MeV. The corrections are:

at 20 deg, 0.040 ± .010,
50 deg, 0.055 ± .010,
80 deg, 0.084 ± .015,
110 deg, 0.090 ± .015.

B. Isobaric Model

1. S-Wave Isobaric Model

According to the "isobaric" model,[6, 28, 29] two possible interactions contribute to the spectrum of the final pions in single-π-production reactions. These are given in Fig. 32. The notation and definition of terms are in Table XV.

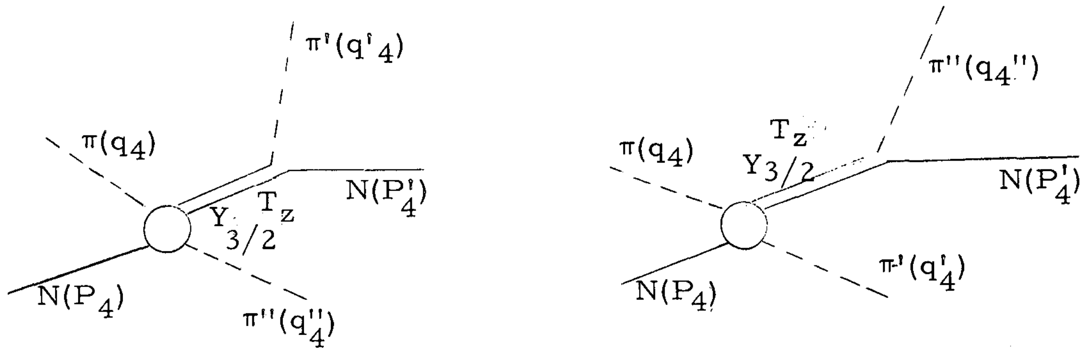

Fig. 32. Diagram corresponding to the two channels of the single-π-production reaction according to the isobaric model.

Lindenbaum and Sternheimer in the early isobar model assumed the two processes in Fig. 32 were incoherent.[30] Bergia, Bonsignori, and Stanghellini (BBS) stated that the two processes in Fig. 32 are not incoherent, but may interfere with each other.[29]

For isotropic production and decay of the isobar, BBS proposed

$$T_{prod} = f(W) \left[\alpha \frac{G(m')^{1/2}}{(m_r - m') - i\, G(m')q'_c} + \beta \frac{G(m'')^{1/2}}{(m_r - m'') - i\, G(m'')q''_c} \right], \quad (31)$$

$$d\sigma_{prod} \propto \frac{1}{IWE} \left| T_{prod} \right|^2 \frac{d^3p'}{E'} \frac{d^3q'}{W'} \frac{d^3q''}{W''} \delta^4(q_4 + P_4 - P'_4 - q'_4 - q''_4). \quad (32)$$

The notations used are described in Table XV.

Let us consider the reaction in the center-of-mass system, as represented in Fig. 33.

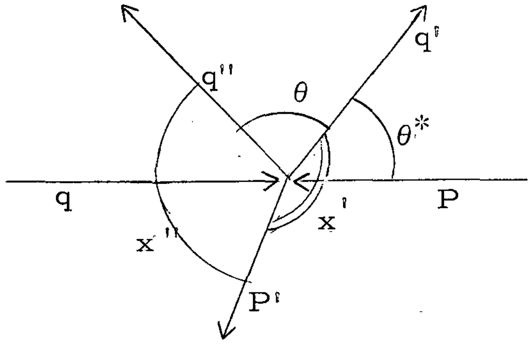

Fig. 33. Center of mass of final state in single π production.

We have

$$d\sigma_{prod} \propto \frac{1}{IWE} \left| T_{prod} \right|^2 \frac{d\bar{p}'\, d\bar{q}'\, d\bar{q}''}{E'\, W'\, W''} \delta^3 (\bar{q}' + \bar{P}' + \bar{q}'')\, \delta\, (E^* - E' - W' - W''). \quad (33)$$

Table XV. Notations for calculation of isobaric model.

A. Isotopic Spin

$Y^{T_z}_{3/2}$ = isotopic spin function for $T = 3/2$ isobar

α = isotopic spin Clebsch-Gordan coefficient for π' as a member of the isobar

β = isotopic spin Clebsch-Gordan coefficient for π' as the recoil particle

B. Kinematics

All quantities are evaluated in the over-all center-of-mass system. Initial-state quantities are unprimed and final-state quantities are primed.

P_4, P, E, and M = 4-momentum, 3-momentum, energy, and mass of nucleons

q_4, q, W, and μ = 4-momentum, 3-momentum, energy, and mass of pions

I = incident flux

E^* = total c. m. energy

C. Isobar Terminology (applies to both primed and double-primed pions)

$m'^2 = (q_4' + P_4')^2$ = total energy squared, in $\pi'N$ center-of-mass frame

q_c' = 3-momentum in $\pi'N$ center-of-mass frame

$\omega' = m' - M$

$\omega_r = (m'_{\text{resonance}} - M) \approx 2.1\ \mu$

f^2 = pseudovector coupling constant

$g = 4 f^2 \omega_r / 3 \approx 0.22/\mu$

$G(m') = g\, q_c'^{\,2}/\omega'$

$D(m') = (m_r - m') - i\, G(m') q_c'$

Using the momentum δ function, we integrate over $d\bar{p}'$. Next we integrate over dq'', using the energy δ function and the identity

$$\int f(t)\ \delta\,(h(t))\,dt = \frac{f(t_0)}{|h'(t_0)|}\ , \tag{34}$$

where t_0 is determined by the equation $h(t_0) = 0$. In this case $h(q'')=0$ is just the conservation-of-energy equation, which reduces to the quadratic equation (35) for $W''(q'')$ in terms of q', W', E^*, and θ, where θ is the angle between π' and π'':

$$W''^2\,(4A^2 - 4q'^2\cos^2\theta) - 4AB\ W'' + (B^2 + 4q'^2\cos^2\theta\ \ \mu''^2) = 0\ ; \tag{35}$$

here $A = E^* - W'$, $\quad (36)$

$$B = A^2 - q'^2 - M^2 + \mu''^2 = E^{*2} - 2E^*W' + \mu'^2 + \mu''^2 - M^2, \tag{37}$$

and $\cos\theta = (B - 2AW'')/2\,q''q'$. $\quad (38)$

The positive square root of the discriminant applies for $-1 \leqslant \cos\theta \leqslant 0$, and the negative root applies for $0 \leqslant \cos\theta \leqslant 1$. If we use Eq. (34), then Eq. (33), after being multiplied by q''/q'', becomes

$$d\sigma \propto \frac{1}{IWE}\, q'^2 dq' d\Omega q'\ \frac{q''^3\,|T_{\text{prod}}|^2\ d\Omega q''}{W'\,|\,(W''^2 - \mu''^2 + (B/2) - AW'')\,W'' + (W''^2 - \mu''^2)(A - W'')|}\ . \tag{39}$$

We divide by $dq'd\Omega q'$ and further reduce the expression to give

$$\frac{d^2\sigma}{dq'd\Omega q'} \propto \frac{q'^2}{IWEW'^2}\ \frac{(W''^2 - \mu''^2)^{3/2}\ |\,T_{\text{prod}}|^2 d\Omega q''}{((BW''/2) - \mu''^2 A)} \tag{40}$$

We must next evaluate the expression $|T_{\text{prod}}|^2$, which is a function of m', m'', q'_c, and q''_c. By expanding the invariant m'^2 in both the over-all c.m. system and the πN c.m. system we get the expressions

$$q_c'^2 = \frac{(m'^2 - \mu'^2 - M^2)^2 - 4\mu'^2 M^2}{4m'^2} \tag{41}$$

and

$$m'^2 = \mu'^2 + M^2 + 2E'W' - 2q'p'\cos\chi' \tag{42}$$

$$= (W''^2 - W'^2) - E'^2 + 2E'W' + \mu'^2 + 2M^2. \tag{43}$$

From Eqs. (40) and (41),

$$\frac{d^2\sigma}{dq'd\Omega q'} \propto \frac{1}{IWE} \frac{q'^2}{W'} \int_{\Omega q''} GG(\theta) \left| T_{prod} \right|^2 d(\cos\theta) d\phi \ , \tag{44}$$

where

$$GG(\theta) = (W''^2 - \mu''^2)^{3/2} / ((B/2)W'' - A\mu'^2) \tag{45}$$

and

$$\left| T_{prod} \right|^2 = \alpha^2 \frac{G(M')}{(m_r - m')^2 + G^2(m')\, q_c'^2}$$

$$+ \beta^2 \frac{G(m'')}{(m_r - m'')^2 + G^2(m'')^2\, q_c''^2}$$

$$+ 2\alpha\beta \left[G(m')G(m'') \right]^{1/2} \frac{(m_r - m')(m_r - m'') + G(m')G(m'')q_c'q_c''}{\left[(m_r - m'')^2 + G^2(m')q_c'^2\right]\left[(m_r - m'')^2 + G(m'')q_c''^2\right]} \ , \tag{46}$$

$$\frac{d^2\sigma}{dT'd\Omega q'} = \frac{W'}{q'} \frac{d^2\sigma}{dq'd\Omega'} \ . \tag{47}$$

The last term of Eq. (46) is the interference term of BBS; $GG(\theta)$ is the phase space factor;

$\frac{d^2\sigma}{dT'd\Omega q'}$ is the quantity we wish to compare with our measured distributions.

2. P-Wave Isobaric Model

The isobar is assumed to be produced in the form $a + b \cos \theta_{N^*}$, where θ_{N^*} is the angle of production of the isobar in the over-all center-of-mass system. For simplicity the decay is taken to be isotropic in the isobar c. m. The ramifications of this assumption are discussed in Sec. VII.B.

Figure 34 shows the coordinate system used. In Fig. 34a, π' is a member of the isobar and in Fig. 34b π' is the recoil particle.

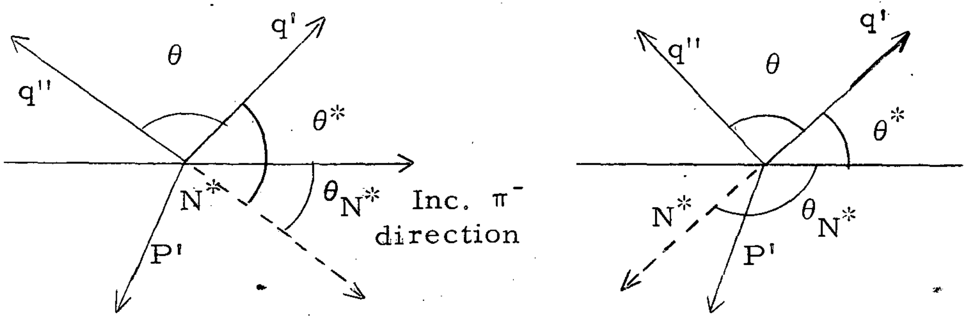

(a) (b)

Fig. 34. Final-state c.m. system for both channels of isobar production.

In Fig. 34(b) the isobar recoils opposite to π'; $\cos \theta_{N^*}$, therefore, is just $-\cos \theta^*$, where θ^* is the π' c.m. angle. In Fig. 34(a) we have

$$\cos \theta_{N^*} = \cos(\pi - \theta) \cos \theta^* + \sin(\pi - \theta) \sin \theta^* \cos((\pi + \phi) - \pi)$$

$$= -\cos\theta \cos\theta^* + \sin\theta \sin\theta^* \cos\phi,$$

where ϕ is the azimuthal angle of π'' with respect to the coordinate system whose z axis lies along π'. If we rewrite Eq. (31) in the form

$$T_{prod} = \alpha A(m', q_c') + \beta B(m'', q_c'') \quad , \tag{48}$$

introducing the $a + b \cos \theta_{N^*}$ dependence requires

$$T_{prod} = \alpha\ A(m', q_c') (a+b) [-\cos\theta \cos\theta^* + \sin\theta \sin\theta^* \cos\phi]$$
$$+ \beta\ B(m'', q_c'') (a - b\cos\theta^*).$$

When we square T_{prod} now we get ϕ-dependent terms. Terms containing $\cos\phi$ are dropped because these integrate out to zero when we integrate over ϕ. The result is

$$|T_{prod}|^2 = \alpha^2 A^2 [a^2+b^2 (\cos^2\theta \cos^2\theta^* + \sin^2\theta \sin^2\theta^* \cos^2\phi)$$
$$-2\ a\ b \cos\theta \cos\theta^*]$$
$$+ \beta^2 B^2 (a^2+b^2 \cos^2\theta^* -2ab \cos\theta^*)$$
$$+2\ \alpha\beta\ \mathrm{Re}\ A^* B[a^2+b^2 \cos\theta \cos^2\theta^* + ab\ (-\cos\theta^* - \cos\theta \cos\theta^*)]. \quad (50)$$

3. Computer Program and Fit to Data

"ZIGGY," a program written in FORTRAN for the IBM 7090 computer, performs the calculation of $d^2\sigma/dq'd\Omega$ and $d^2\sigma/dT'd\Omega'$ as given by phase-space distributions and the s- and p-wave isobar models. It first does this at equal intervals of energy T' from $T' = 0$ to T_{max}, the maximum c.m. energy allowed. It then integrates $d^2\sigma/dT'd\Omega'$ over T' and Ω' to determine the overall normalization of each function calculated. The program next calculates the same quantities for the measured data points and uses the IBM SHARE routine VARMINT to make a least-squares fit to the functions themselves and to linear combinations of the functions.

The supposed linear combinations are actually introduced into the T matrix in Eq. (44), e.g., for a phase-space background and an s-wave isobar model capable of interfering with each other, I assume a T matrix of the form

$$T_{prod} = X_1 + X_2 \exp(iX_3)(\alpha A + \beta B).$$

In this case, since A and B are complex quantities, we get upon squaring, terms of the form

$$2X_1X_2\,(\cos X_3\,\mathrm{Re}(\alpha A+\beta B) + \sin X_3\,\mathrm{Im}(\alpha A+\beta B)).$$

An assumption of interference here introduces into the calculation the complex quantities themselves and not just a product of two complex quantities. The program varies X_1, X_2, and X_3 so that the χ^2 of the fit to the data[33] is a minimum. Several types of T_{prod} were assumed and fits were obtained for both $T_{init} = 1/2$ and $T_{init} = 3/2$. They are described in Table XVI. The results are given in Table XVII. The total cross section as determined from the fitting parameters and the calculated normalizations are also listed.

In Table XVII,

x(2) is the s-wave isobar amplitude in fits 1 to 10,

x(1) is the phase-space background amplitude in 1 to 10, and

x(3) is either a phase angle in fits 4, 9, and 12 or the coefficient of $\cos\theta_{N^*}$ in fits 5 and 10 (p wave).

Table XVI. Description of models used to fit π^+ data.

Fit No.		Model	$\lvert T_{prod}\rvert^2$ [a]
T=1/2	T=3/2		
1	6	phase space	$x^2(1)$
2	7	s-wave isobar	$x^2(2)\ I_T^{\,2}$
3	8	s-wave isobar + noninterfering phase-space background.	$x^2(1) + x^2(2)\ I_T^{\,2}$
4	9	s-wave isobar + interfering phase-space background	$\lvert x(1) + x(2)\ e^{ix(3)}\ I_T\rvert^2$
5	10	p-wave isobar	$\lvert I_T(x(2) + x(3)\cos\theta_N)\rvert^2$
11	11	two T states--without interference	$x^2(1)\ I_{3/2} + x^2(2)\ I_{1/2}$
12	12	two T states--with interference	$\lvert x(1)\ I_{3/2} + x(2)\ e^{ix(3)} I_{1/2}\rvert^2$

[a] $I_T = \alpha_T A + \beta_T B$, as described in Eq. (31).

Table XVII. Results of fit to π^+ data described in Table XVI.

		365 MeV, 21 data points						432 MeV, 20 data points					
	Fit No.	x(1)	x(2)	x(3)	χ^2[a]	Prob.[b]	σ_{Tot}[c]	x(1)	x(2)	x(3)	χ^2[a]	Prob.[b]	σ_{Tot}[d]
T = 1/2	1	0.88			318		1.66	0.96			631		3.05
	2		1.96		53	10^{-4}	2.63		0.97		162		3.67
	3	0.30	1.87		47	10^{-4}	2.56	0.46	1.33		131		3.74
	4	-0.30	1.55	-0.44	29	.05	2.39	0.39	1.28	-1.08	79		4.03
	5		1.97	0.13	47	10^{-4}	2.69		1.45	- .06	157		3.62
T = 3/2	6	0.88			318		1.66	0.96			631		3.05
	7		2.27		1287		1.39		2.04		826		3.30
	8						e	0.80	1.27		551		3.39
	9	1.05	0.68	1.04	25	.12	2.48	1.03	0.67	1.89	83		4.26
	10		3.17	.43	586		0.41		1.97	- .27	810		3.03
T = 1/2, 3/2	11						e	1.25	1.74		89		2.98
	12	2.62	0.83	1.70	725		1.16	0.34	1.53	-1.45	141		3.58

a. Ref. 33. Expected χ^2 = number of degrees of freedom = number of data points - number of parameters.

b. The probability is not listed if less than 10^{-4}.

c. Measured cross section 2.39±0.20.

d. Measured cross section 3.97±0.20.

e. Fitting program could not reach a minimum for positive values of $x^2(I)$.

REFERENCES

1. G. F. Chew and F. E. Low, Phys. Rev., 101, 1570 (1956).
2. Saul Barshay, Phys. Rev. 103, 1102 (1956);
   Jerrold Franklin, Phys. Rev. 105, 1101 (1957);
   Leonard S. Rodberg, Phys. Rev. 106, 1090 (1957);
   Emil Kazes, Phys. Rev. 107, 1131 (1957).
3. V. G. Zinov and S. M. Korenchenko, Zh. Eksperim. i Teor. Fiz. 34, 301 (1958) Soviet Phys. JETP English Transl. 34 (7), 210 (1958).
4. Walton A. Perkins, III, John C. Caris, Robert W. Kenney, and Victor Perez-Mendez, Phys. Rev. 118, 1364 (1960).
5. Leonard S. Rodberg, Phys. Rev. Letters 3, 58 (1959).
6. V. V. Anisovich, Soviet Phys. JETP English Transl. 12, 71 (1961);
   V. V. Anisovich, Soviet Phys. JEPT English Transl. 12, 946 (1961).
7. Owen Chamberlain, Optics of High Energy Beams, Ann. Rev. Nucl. Sci. 10, 161 (1960).
8. Marvin Rich and Richard Madey, Range-Energy Tables, University of California Radiation Laboratory Report UCRL-2301, March 1954 (unpublished).
9. Hugo R. Rugge, Scattering of Negative Pions on Protons at 310 MeV: Differential and Total Cross Sections and Phase-Shift Analysis (Thesis), Lawrence Radiation Laboratory Report UCRL-10252, May 1962 (unpublished).
10. Duane D. Newhart, Victor Perez-Mendez, and Willian L. Pope, Liquid Hydrogen Target, Lawrence Radiation Laboratory Report UCRL-8857, August 1959 (unpublished).
11. R. H. Dalitz, Proc. Phys. Soc. (London) A64, 667 (1951).
12. Robert Squire, Characteristics of the Production of Neutral Mesons near Threshold in p-p Collisions (Thesis) University of California Radiation Laboratory Report UCRL-3137, Sept. 1955 (unpublished).
13. John C. Caris, Charge-Exchange Scattering of Negative Pions by Hydrogen at 230, 260, 290, 317, and 371 MeV (Thesis), Lawrence Radiation Laboratory Report UCRL-9048, March 1960 (unpublished).

14. John H. Atkinson, Jr., and Beverly Hill Willis, High-Energy Particle Data, Volume II, University of California Radiation Laboratory Report UCRL-2426 (Rev.), June 1957 (unpublished).

15. Hans A. Bethe and Julius Ashkin, Passage of Radiations through Matter, in *Experimental Nuclear Physics* (John Wiley and Sons, Inc., New York, 1953), Vol. I, p. 329.

16. Walter H. Barkas and Arthur H. Rosenfeld, Data for Elementary Particles, Lawrence Radiation Laboratory Report UCRL-8030 (Rev.), Oct. 1, 1961 (unpublished).

17. Donald Harvey Stork, Phys. Rev. 93, 868 (1954).

18. R. M. Sternheimer, Rev. Sci. Instr. 25, 1070 (1954).

19. Charles J. Goebel and Howard J. Schnitzer, Phys. Rev. 123, 1021 (1961).

20. Barry C. Barish, Richard J. Kurz, Paul G. McManigal, Victor Perez-Mendez, and Julius Solomon, Phys. Rev. Letters 6, 297 (1961).

21. Howard J. Schnitzer, Phys. Rev. 125, 1059 (1962).

22. M. E. Blevins, M. M. Block, and J. Leitner, Phys. Rev. 112, 1287 (1958).

23. Barry C. Barish, A Study of the Reaction $\pi^- + p \rightarrow \pi^- + \pi^0 + p$ at 310 and 377 MeV (Thesis) Lawrence Radiation Laboratory Report UCRL-10470, Aug. 1962 (unpublished).

24. Richard J. Kurz, Differential Distributions of Neutrons in Inelastic π^--p Interactions at 374, 417, and 454 MeV (Thesis), Lawrence Radiation Laboratory Report UCRL-10564, Dec. 1962.

25. Janos Kirz, Joseph Schwartz, and Robert D. Tripp, Phys. Rev. 126, 763 (1962).

26. Alexander Abashian, Norman E. Booth, and Kenneth M. Crowe, Phys. Rev. Letters 5, 258 (1960).

27. Alexander Abashian, Norman E. Booth, and Kenneth M. Crowe, Phys. Rev. Letters 7, 35 (1961);
Bipin R. Desai, Phys. Rev. Letters 6, 497 (1961).

28. N. N. Khuri and S. B. Treiman, Phys. Rev. 113, 1640 (1959).

29. S. Bergia, F. Bonsignori, A. Stanghellini, Nuovo Cimento 16, No. 6 (1960).

30. S. J. Lindenbaum and R. B. Sternheimer, Phys. Rev. 105, 1874 (1957); 106, 1107 (1957); 109, 1723 (1958).

31. V. Alles Borelli, S. Bergia, E. Perez-Ferreira, and P. Waloschek, Nuovo Cimento 14, 211 (1959);
I. Derado and N. Schmitz, Phys. Rev. 118, 309 (1961);
I. Derado, G. Lütjens, and N. Schmitz, Ann. Physik 4, 103 (1959).

32. Lester K. Goodwin, Robert W. Kenney, and Victor Perez-Mendez, Phys. Rev. 122, 655 (1961).

33. Harald Cramèr, Mathematical Methods of Statistics (Princeton University Press, Princeton, N. J., 1946);
Peter Cziffra and Michael Moravcsik, A Practical Guide to the Method of Least Squares, Lawrence Radiation Laboratory Report UCRL-8523, June 1959 (unpublished).

34. Janos Kirz, Joseph Schwartz, and Robert D. Tripp, A Preliminary Study of the Reaction $\pi^- p \rightarrow \pi^+ \pi^- n$, Lawrence Radiation Laboratory Physics Note UCID-407, June 1962 (unpublished).

35. L. F. Cook, Jr., and B. W. Lee, Phys. Rev. 127, 297 (1962);
J. S. Ball, W. R. Frazer, and M. Nauenberg, Phys. Rev. 128, 478 (1962).
S. Mandelstam, J. E. Paton, R. F. Peierls, and A. Q. Sarker, Ann. Phys. (New York) 18, 198 (1962).

36. Yu. A. Batusov, S. Abunyatov, V. M. Sidorov, and V. A. Yarba, in Proceedings of the 1960 Annual International Conference on High-Energy Physics at Rochester (Interscience Publishers, Inc., New York, 1960), pp. 64 and 76.

37. R. Turley, Contributions a l'Etude des Reactions $\pi^- + p \rightarrow \pi^0 + n$ et $\pi^- + p \rightarrow \pi^0 + \pi^0 + n$ aux Energies des Maxima de la Section Efficace, Totale de l'Interaction π^- Nucleon dans l'Etat de Spin Isobarique T = 1/2 (thèse), Commissariat a l'Energie Atomique Rapport, C. E. A. 2136, 1962 (unpublished).

38. T. D. Blokhintseva, V. G. Grebinnik, V. A. Zhukov, G. Libman, L. L. Nemenov, G. I. Selivanov, and Y. Jung-Fang, Soviet Physics JETP (English Transl.) 15, 629 (1962).

This report was prepared as an account of Government sponsored work. Neither the United States, nor the Commission, nor any person acting on behalf of the Commission:

A. Makes any warranty or representation, expressed or implied, with respect to the accuracy, completeness, or usefulness of the information contained in this report, or that the use of any information, apparatus, method, or process disclosed in this report may not infringe privately owned rights; or

B. Assumes any liabilities with respect to the use of, or for damages resulting from the use of any information, apparatus, method, or process disclosed in this report.

As used in the above, "person acting on behalf of the Commission" includes any employee or contractor of the Commission, or employee of such contractor, to the extent that such employee or contractor of the Commission, or employee of such contractor prepares, disseminates, or provides access to, any information pursuant to his employment or contract with the Commission, or his employment with such contractor.